

April 2022

**IEA Wind TCP Task 40**

**Downwind Turbine Technologies  
Technical Report**



**iea wind**



**International Energy Agency Wind Technology Collaboration Programme**

**Task 40 Downwind Turbine Technologies, Technical Report**



Technical recommendations for Considering of Future Electrotechnical Commission (IEC) 61400-1 Standard.

April 2022

## TECHNICAL REPORT

International Energy Agency Wind Technology Collaboration Programme  
Task 40 Downwind Turbine Technologies Technical Report

Prepared for the International Energy Agency Wind Implementing Agreement

Edited by:

Shigeo Yoshida

Kyushu University, Research Institute for Applied Mechanics

6-1 Kasugakoen, Kasuga, Fukuoka, 816-8580, Japan

Saga University, Institute of Ocean Energy

1 Honjomachi, Saga, Saga, 840-8502, Japan

With contributions from:

Germany:

- (Fraunhofer Institute for Wind Energy Systems) Bernhard Stoevesandt, Bastian Dose, Hamid Rahimi, Elia Daniele, Leo Hoening, Johannes Theron
- (Technical University of Munich) Carlo L. Bottasso, Helena Canet, Carlo Sucameli, Thorsten Lutz,

Japan:

- (Class NK) Tomoya Iwashita
- (National Institute of Advanced Industrial Science and Technology) Tetsuya Kogaki, Shigemitsu Aoki
- (Hitachi) Mitsuru Saeki, Soichiro Kiyoki, Nobuo Namura, Yasuo Osone, Yusuke Otake, Shinya Tadano, Shinya Ohara, Shigehisa Funabashi
- (Research Center for Computational Mechanics) Noriki Iwanaga
- (The University of Tokyo) Atsushi Yamaguchi
- (Wind Energy Institute of Tokyo) Masataka Owada, Yoshitaka Totsuka

Spain:

- (Centro Nacional de Energias Renovables) Xabier Munduate, Mikel Iribas Latour, Antonio Ugarte, Beatriz Mendez
- (X1Wind) Alex Raventos, Carlos Cosanovas, Rocio Torres

United States:

- (Boulder Wind Consulting) Sandy Butterfield
- (National Renewable Energy Laboratory) Nick Johnson, Pietro Bortolotti, Rick Damiani, Fabian Wendt, Tyler Stehly, Ryan Wiser
- (NextEra) Dan Brake
- (Otherlab) Sam Kanner, James Reeves
- (University of Massachusetts Amherst) James Manwell
- (University of Texas Dallas) Todd Griffith
- (University of Virginia) Eric Loth

(Alphabetic order in countries and organizations.)

April 2022

The International Energy Agency (IEA) Wind Technology Collaboration Programme (TCP) functions within a framework created by the IEA. Views, findings and publications of IEA Wind do not necessarily represent the views or policies of the IEA Secretariat or of its individual member countries. IEA Wind is part of IEA's TCP.

## PREFACE

This technical report has been developed to provide the best available recommendations on this topic, to reduce the risks in the design and deployment of downwind turbines and accelerate the growth of wind energy production in these areas. This document addresses many special issues that must be considered over the lifetime of the present and future super large and/or floating offshore downwind turbines.

This technical report provides a series of recommendations based on Task 40 research results that should be considered in future standards-making activities for IEC 61400-1 etc. While these recommendations are preliminary in nature and require further validation, many of the results suggest the aeroelastic models for the aerodynamic interaction between the rotor and the tower (well-known as tower shadow effect) and the nacelle, load calculation conditions for passive (free) yawing in storms, etc. It is recommended that both modeling and design conditions be used to design and validate downwind turbines.

Table 1 IEA Wind Task 40 Participants during this period (2019-2021)

Country	Active Organizations
Germany	Fraunhofer Institute for Wind Energy Systems (IWES)
Japan	National Institute of Advanced Industrial Science and Technology (AIST) Class NK (NK) Hitachi Kyushu University (KU) Research Center of Computational Mechanics (RCCM) (2020~) The University of Tokyo (UTokyo) Wind Energy Institute of Tokyo (WEIT)
Spain	Centro Nacional de Energias Renovables (CENER) (~2019) X1 Wind
United States	Boulder Wind Consulting (BWC) National Renewable Energy Laboratory (NREL) Otherlab (2020~) University of Texas at Dallas (UTD) (~2019) University of Massachusetts (UMass) (~2019) University of Virginia (UVA)

Alphabetic order.

### Contracting Parties

- Germany: Bundesministerium für Wirtschaft und Klimaschutz (BMWK)
- Japan: New Energy and Industrial Technology Development Organization (NEDO)
- Spain: Centro Nacional de Energias Renovables (CENER) (~2019), X1Wind
- United States: National Renewable Energy Laboratory (NREL)

Shigeo Yoshida, Operating Agent  
IEA Wind TCP, Task 40  
[www.ieawind.org](http://www.ieawind.org)

Masataka Owada, Co-operating Agent  
IEA Wind TCP, Task 40  
[www.ieawind.org](http://www.ieawind.org)

April 2022

### DISCLAIMER:

IEA Wind TCP functions within a framework created by the IEA. The views, findings and publication of this report do not necessarily represent the views or policies of the IEA Secretariat or of all of its individual member countries.

## TABLE OF CONTENTS

PREFACE .....	4
TABLE OF CONTENTS .....	5
ABBREVIATIONS .....	7
EXECUTIVE SUMMARY .....	8
1. BACKGROUND AND OBJECTIVES .....	9
1.1 Introduction .....	9
1.2 Objectives .....	12
2. TOWER SHADOW MODELS FOR BLADE AERODYNAMIC LOADS .....	13
2.1 Introduction .....	13
2.2 Recommendations .....	13
2.3 Load Equivalent Tower Shadow Model .....	14
2.4 Dynamic Stall Model for Tower Shadow Effect .....	17
2.5 Tower Shadow Model for System Engineering .....	22
3. TOWER SHADOW MODELS FOR TOWER AERODYNAMIC LOADS .....	24
3.1 Information .....	24
3.2 Recommendations .....	24
3.3 Average Tower Load .....	24
3.4 Dynamic Tower Load .....	31
4. NACELLE BLOCKAGE EFFECT .....	37
4.1 Introduction .....	37
4.2 Recommendation .....	37
4.3 CFD Outlines .....	37
4.4 CFD Results .....	38
4.5 Conclusion .....	40
5. PASSIVE YAW IDLING MODEL AND CONDITIONS .....	41
5.1 Introduction .....	41
5.2 Recommendation .....	41
5.3 Validation by the Measurement .....	41
5.5 Conclusions .....	44
6. SCALING BENEFITS OF DOWNWIND TURBINES .....	46
6.1 Introduction .....	46
6.2 Methodology .....	46
6.3 Optimization Conditions .....	48
6.4 Results and Discussion .....	49
6.5 Conclusions .....	51
7. FURTHER OPPORTUNITIES OF DOWNWIND TURBINES .....	52
7.1 Introduction .....	52
7.2 Methodology .....	52
7.3 Optimization Results .....	53
7.4 Sensitivity Studies .....	56
7.5 Conclusions .....	57
8. CONCLUSIONS/RECOMMENDATIONS .....	59
APPENDIX .....	60
A.1 2 MW Baseline Model .....	60
A1.1 Outline .....	60
A1.2 Model Data .....	60
A.2 Field Test Data of a 2 MW Downwind Turbine .....	62
A2.1 Outline .....	62
A2.2 Measurement Data .....	62

REFERENCE..... 64

**ABBREVIATIONS**

ADM	Actuator Disc Model
AEP	Annual Energy Production
AIST	National Institute for Advanced Industrial Science and Technology (Japan)
BEM	Blade-Element and Momentum (Method)
BLH	Boundary Layer Height
BMWK	Bundesministerium fur Wirtschaft und Klimaschutz
BOS	Balance of Station
BWC	Boulder Wind Consulting (USA)
CENER	National Renewable Energy Centre/Centro Nacional de Energias Renovables (Spain)
CFD	Computational Fluid Dynamics
CG	Center of Gravity
DEL	Damage Equivalent Load
DLC	Design Load Case
DT	Downwind Turbine
EM	Engineering Model
ETM	Extreme Turbulence Model
EWM	Extreme Wind Model
FCR	Fixed-Charge Rate
FOWT	Floating Offshore Wind Turbine
IEA	International Energy Agency
IEC	International Electrotechnical Commission
IWES	Fraunhofer Institute for Wind Energy Systems (Germany)
KU	Kyushu University (Japan)
LCOE	Levelized Cost of Electricity
LE	Leading Edge
MDAO	Multi-Disciplinary Analysis and Optimization
NREL	National Renewable Energy Laboratory (USA)
PSD	Power Spectral Density
OPEX	Operation and Maintenance Expenditure
RCCM	Research Center for Computational Mechanics (Japan)
RMS	Root Mean Square
RNA	Rotor-Nacelle Assembly
SUMR	Segmented Ultralight Morphing Rotor
TCC	Turbine Capital Cost
TCP	Technology Collaboration Programme
TE	Trailing Edge
TI	Turbulence Intensity
TSR	Tip Speed Ratio
UG	University of Glasgow (UK)
UMass	University of Massachusetts (USA)
UTokyo	The University of Tokyo (Japan)
UTD	University of Texas at Dallas (USA)
UVA	University of Virginia (USA)
WEIT	Wind Energy Institute of Tokyo (Japan)
WISDEM	Wind-Plant Integrated System Design and Engineering Model

## EXECUTIVE SUMMARY

Downwind turbines, which have rotors behind the towers, are gathering attention due to their technical advantages toward the reduction of the levelized cost of electricity (LCOE) and deployment of modern/future wind turbines, in spite upwind turbines have been predominant throughout the decades of commercial wind turbine history.

The advantages of downwind turbines include the requirement of the stiffness of the blades. Downwind turbines allow longer and lighter blades with the lower requirements for the stiffness of the blades. And the passive yawing (free yawing) can reduce the loads of downwind turbine in extreme conditions. In addition to that, yawing stability is also promising for the safety to reduce the load and the cost of super large wind turbines. And there some floating offshore wind turbine concepts are assuming downwind turbine, which is advantageous in the stability.

Although, there are numbers of promising features are available by the downwind turbines, there are some problems. Tower shadow effect, which is the aerodynamic interaction between the rotor and the tower, is one of the well-known problems of downwind turbine.

The goal of the document is provided existing industry and academic best practices to help ensure that best quality of downwind turbines.

This document consists with the following chapters.

Chapter 1: Background and the objectives of the present report.

Chapter 2: Tower shadow models for blade dynamic loads

Chapter 3: Tower shadow models for tower loads

Chapter 4: Nacelle blockage effect

Chapter 5: Passive yaw idling

Chapter 6: Scaling benefits of downwind turbines

Chapter 7: Further opportunities of downwind turbines

Chapter 8: Conclusions

Chapters 2~5 provide recommendations for the design and analysis of downwind turbines, and Chapter 6 provides the perspectives and potential applications of downwind turbines. And, some further research opportunities of downwind turbines are recommended in Chapter 7.

This report has been developed to provide the best available recommendations on this topic, to reduce the risks in design and deployment of downwind turbines, and to accelerate the growth of wind energy production in these areas. This document addresses many special issues that must be considered over the lifetime of the present and future super large and/or floating offshore downwind turbines.

## 1. BACKGROUND AND OBJECTIVES

### 1.1 Introduction

#### 1.1.1 Modern History of Downwind Turbines (1940 ~ 85)

There is a rich history of devices invented to extract energy from wind dating back 2000 years in China, 700 years in Persia and over the past 100 years using a deeper understanding of aerodynamics to achieve greater performance. Spera [1], Hau [2], and Manwell [3] et al all describe a rich history of wind turbine design. But prior to 1940 designs mostly used aerodynamic drag to apply pressure flat surfaces for turning rotors. The Dutch were the first to use airfoils on blades. As the science of aerodynamics and fluid dynamics evolved it became clear how to improve performance while saving material expense. Betz [4] was the first to apply mathematical theory to modeling of optimum power production from a wind turbine using fluid momentum theory. His analysis defined the wake shape for optimum power extraction for a given swept area, but not the blade geometry to achieve that wake shape. Many different rotor designs can achieve near optimum performance for the same rotor diameter in the case of horizontal axis turbines. From the standpoint of minimizing LCOE engineers want to minimize the cost of rotors while maximizing the performance. This naturally leads engineers to seek an optimum balance of minimum blade weight for a given rotor diameter. In recent history horizontal axis turbines have proven to be the easiest to achieve the lowest cost of energy using the lowest weight per swept area. Driven to minimize LCOE designers found that horizontal axis turbines with higher tip speeds required less blade projected area to achieve Golding [5] suggested optimum performance. Blades that once looked like rotating sails began to look more like airplane wings which took advantage of low drag and high lift. This approach leads to the long, slender tapered blades.

In 1941 Palmer Putnam (described by Spera [1]) designed the Smith-Putnam 1,250 MW two bladed downwind turbine shown in Figure 1. His design straight blades for simplicity plus downwind hinged blades for load relief. In 1945 the German designer Hutter [6] designed very high tip speed, low solidity downwind turbines shown in Figure 2. Hutter did not compromise on blade geometry as Putnam did, but he used a downwind rotor for load relief and cost reduction, for the same reasons Putnam chose downwind. In 1958 the French Type Nerpic 1.1 MW was installed. This was a three bladed downwind turbine. In 1974, the 100 kW John Brown turbine was installed in the Orkney Islands. These early historical downwind designs were only the first in a long list of downwind turbine designs that were either experimental or commercial. Most of the early technical thought leaders favored downwind turbines. The list below chronicles many, but not all of them.

Table 2 Historical downwind turbines (1940-85)

Year	Manufacturer/Wind Turbine	Rated Power	Num. of Blades
1941	Smith Putnam	1250 kW	2
1942	Aeromotor	50 kW	2
1945	Hutter	100 kW	2
1958	Neyrpic	1100 kW	3
1974	John Brown Orkney Island	100 kW	3
1977	NASA MOD-0	100 kW	2
1979	NASA MOD-1	2000 kW	2
1978	Hamilton Standard WTS-4	4000 kW	2
1978	WTS-3	3300 kW	2
1985	US Wind Power (later Kenetech)	75 kW	3
1980	ESI	75 kW, 300 kW	2
1980	Carter	25 kW, 300 kW	2
1987	Enertech	8 kW, 40 kW	3
1988	Kaman Aerospace	40 kW	2



Figure 1 Smith-Putnam 1,250 MW two-bladed downwind turbine.



Figure 2 Hutter 100 kW two-bladed downwind turbine.

When engineers after 1945 set out to design modern wind turbines they wanted to capitalize on all that had been learned from the rotor craft industry. Helicopter design had produced remarkably high-performance, light weight rotors. The key to successful helicopters was very flexible rotors plus active pitch controls. The ability of blades to seek a balance between bending moments caused by thrust and counteracting moments caused by centrifugal forces acting on the blades as they deflect out of the rotor plane of rotation has been used by every helicopter since. But the simplicity and cost of wind turbine designs were far more important goals. Designers could not afford the complexity of helicopter rotor designs, but they could capitalize on the fundamental principles like downwind coning for load relief. Furthermore, downwind turbines offered the ability to self-align with wind direction passively. They enabled downwind coning which balanced thrust loads with centrifugal loads on the blade, drastically reducing the average blade root bending loads. Balancing centrifugal bending moments with thrust bending moments was what enabled helicopters to eliminate blade root bending moments and hence lighter blades. This strategy was what lead Smith and Putnam to design hinged blades for their 1.25 MW two bladed downwind turbine in 1945. But greater flexibility for reduced loads results in greater tip deflection. These two factors allow reduce weight with minimal loss to performance. Increased tower clearance is another benefit of downwind rotors. As thrust loads increase, the blades will deflect downwind, creating increased tower clearance. In an upwind configuration tower clearance decreases with increased wind speed and corresponding thrust. Therefore, IEC standards have minimum tower clearance requirements. With downwind turbines blade can be made more flexible because they have larger tower clearance. This will reduce blade weight and hence cost. The design balance that must be reached is how much flexibility can be designed into the rotor. Most of US designers and the US Department of Energy researchers as well as most international researchers, felt the path to lowest COE for large commercial turbines was using the advantages downwind rotors had to offer to go directly to megawatt scale light weight downwind turbines. All design configuration trade off studies concluded that downwind turbines would result in the lowest cost of energy for large scale turbines purely on a technical basis.

Early designers faced three technical challenges, but only two were unique to downwind turbines, noise generated by tower shadow and possible impulsive loading on blades from the tower shadow. In most other

respects downwind design challenges are shared by upwind turbines, such as performance optimization, rotor dynamics, design loads, controls, etc.

#### (1) Tower shadow loads

There was some concern that the tower shadow would induce dominant flatwise fatigue loads. Research by many analysts has shown that turbulence loading dominates the fatigue loads. Couturier et al. [7] shows a comparison of predicted flap loads for four different cases using two dynamic analysis codes.

#### (2) Tower shadow noise

One of NASA's early prototype 2 MW downwind turbines, the MOD-1, produced significant tower shadow impulsive noise because of its very high tip speed (140 m/s, almost twice what is common practice today), massive tower and low tower clearance. Spera, et al (a) describes in Chapter 7 of his text research into the physics of the tower shadow noise generation. Since then, it has been demonstrated that one effective solution was to reduce the rotor speed which reduced aerodynamic pressure on the blades and dramatically reduced the noise signature. This has been used by all turbines since, including upwind turbines. But many other small commercial downwind turbines with similar high tip speeds also produced tower shadow noise, though none at the same magnitude as the MOD-1. So, the reputation of downwind turbine was well earned by this early class of turbines and they were dismissed by the shrinking US and steadily growing European market before they had a chance to prove their other benefits.

#### (3) Adequate design tools

Designers lacked proper design tools and a detailed understanding of atmospheric turbulence. They also lacked reliable design process and design standards. This was not unique to downwind turbines. Both upwind and downwind turbines suffered from a lack of accurate analysis capabilities. Prior to 1995 the design tools available to designers were not able to accurately predict dynamic rotor loads driven by turbulence, especially for control induced large deflection combined with turbulence. Modern multi-physics design tools can predict non-linear behavior and detailed unsteady aerodynamic behavior such as dynamically induced turbulence loads, control induced loads or combinations of both. This is a dramatic shift from what engineers had available in the late 1970s and 1980s.

### 1.1.2 Technical Challenges Since 1950

Several factors have changed the challenges faced by early designers of downwind turbines.

- 1) Dramatic improvements in analytical capability – advanced computing power has enabled multi-physics models with computational fluid dynamics interacting with structural dynamic models to model more accurately unsteady aerodynamic forces, characterize turbulence in greater detail and predict dynamic loads.
- 2) Turbine design capabilities have advanced dramatically. Designers are now using more sophisticated blade aerodynamic designs, advanced material, and advanced controls to achieve far more sophisticated rotor designs with more accurate prescribed flexibility that can withstand complex turbulence and large range of design load cases with greater precision.
- 3) The scale of turbines has dramatically increased, making rotor weight and cost ever more important and atmospheric turbulence the dominant contributor to dynamic loads.

### 1.1.3 New Technical Challenges for Downwind Turbines

The combined result of 40 years of design experience has led to a greater understanding of the issues that once challenged downwind turbines.

The path to lower cost wind energy is clearly larger turbines, especially for offshore turbines. Turbines have scaled up to greater than 150 m diameter onshore and will soon be larger than 220 m offshore. This would not have been possible without greater blade flexibility. But upwind turbines are limited in how far they can increase flexibility in the quest for further dynamic load relief. Downwind rotor designs remove one of the constraints on tower clearance, which allows downwind coning and greater tip deflections. This results in a reduced average bending moment and greater flexibility, both of which will be essential for future innovations in large turbine

designs. Advanced control strategies for wind plants may include wake steering about both yaw and tilt axes. This will not be possible with upwind turbines.

## **1.2 Objectives**

Among designers all over the world, there is renewed interest in downwind turbines because downwind turbines can remove constraints and enable advanced designs. However, turbine original equipment manufacturers and developers may be reluctant to adopt downwind designs without adequate consensus that the technical basis is sound and low risk. The shared international research builds confidence in that technical basis and validates the benefits. IEA Wind offers a unique objective forum of technical experts and researchers to review and compare results. IEA Wind is viewed as a highly credible organization of internal technical peers. IEA Wind has been producing comprehensive studies and reports related to wind energy since 1985. IEA Wind Task 40 is focused updating the industry's collective technical understanding and attributes of downwind turbines. This task is intended to collect the results of ongoing international research into a comprehensive body of information that can inform the wind industry.

The objective of Task 40 is to coordinate international research and investigate the benefits of downwind turbine technology toward the reduction of LCOE and proliferation of onshore and offshore wind plants. The Task is designed to capitalize on past experiences and recent demonstration's results as well as recently developed computational capabilities.

The focus will include onshore and offshore wind turbine applications while investigating the relevant design conditions where downwind turbines might offer advantages. Key research aspects that will be studied include dynamic response, loads, controls, developing analysis models, and impact on LCOE and so on.

The task will include an objective, harmonized approach to assessing the LCOE of downwind turbines based on select baseline turbine models and methods accepted by the Participants. We are expecting to research and investigate the benefits of downwind turbine technology with many researchers from many countries.

The following chapters will address technical and economic benefits of downwind turbines in a comprehensive way.

## 2. TOWER SHADOW MODELS FOR BLADE AERODYNAMIC LOADS

### 2.1 Introduction

Aerodynamic interaction between the rotor and tower is significant for downwind turbines as blades passing through the low wind speed region behind the tower.

CFD with high fidelity model of Hitachi HTW2.0-80 (2 MW, 80 m) downwind turbine, at 8.6 m/s steady winds, 1.6 degrees of blade pitch angle. The CFD was conducted using OpenFOAM [8] with 16 million of cells per blade as shown in Figure 3. Figure 4 shows the blade root bending moments. There appear the impulsive loads when one of the three blades is passing behind the tower. The load fluctuation can affect the fatigue and extreme loads of the wind turbine. This is called as “tower shadow effect”. Therefore, modeling of the phenomena is essential for the design of downwind turbines. Appropriate tower shadow models in BEM simulation are proposed in this chapter.

However, the tower shadow effect is less significant for the real flexible wind turbines in turbulent wind conditions as shown in Appendix A.2.

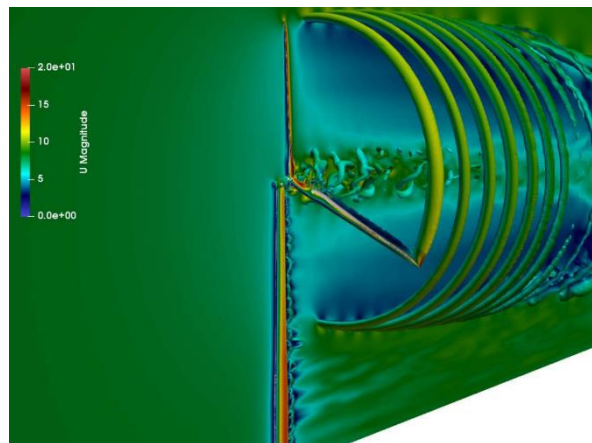
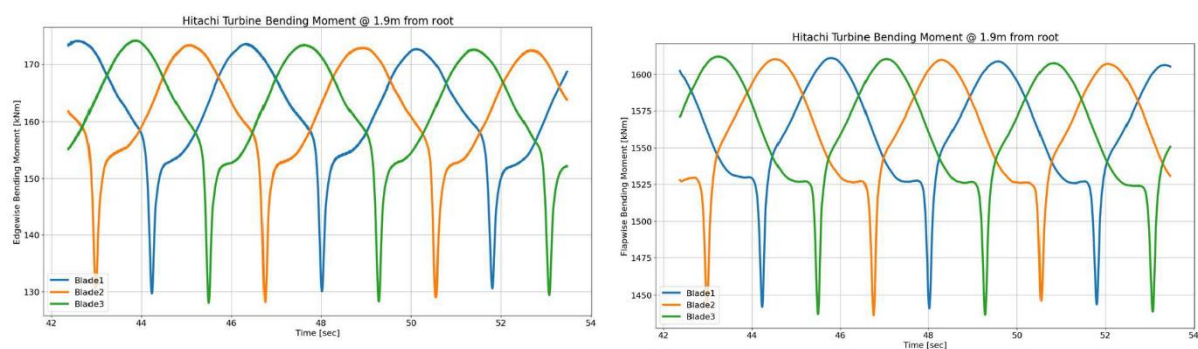


Figure 3 CFD result



(a) Edgewise

(b) Flapwise

Figure 4 CFD result: Blade root aerodynamic bending moment

### 2.2 Recommendations

Appropriate tower shadow models for BEM are recommend for blade aerodynamic loads are different in accordance with the size and rotor speed.

(1) Blade loads of large-scale downwind turbines

Load equivalent tower shadow model in Section 3 is recommended.

(2) Blade loads of small downwind turbines

Dynamic tower shadow model in Section 4 is recommended for small wind turbines. The dynamic effects are

negligible for large scale wind turbines.

## 2.3 Load Equivalent Tower Shadow Model

### 2.3.1 Background

Former tower shadow models in BEM have been defined based on the wake wind speed profile provided by CFD or wind tunnel tests on an isolated column (3D) or cylinder (2D). Those approaches ignore interactions between rotor and tower, rotor-tower CFD is expected to express the phenomena well. But it is impossible to calculate the full set of load cases by rotor-tower CFD, because huge numbers of simulations for aeroelastic models are necessary as mentioned above.

Considering these circumstances, a practical modeling method, which considers rotor-tower interaction appropriately, was investigated and proposed in the present study.

This section is based on Yoshida and Kiyoki [9], Yoshida and Kiyoki [10].

### 2.3.2 Recommendation

#### (1) Load Equivalent Tower Shadow Model for aeroelastic Simulation

The wind speed profile behind the tower is often defined as the bell-shaped model defined by the following parameters.

$$\frac{V(x, y)}{V_0} = 1 - e \cdot \cos^2\left(\frac{\pi y}{WD}\right) \quad (1)$$

where,

$$\frac{e(x)}{e(x_{ref})} = \left(x/x_{ref}\right)^{-1/2}$$

$$\frac{W(x)}{W(x_{ref})} = \left(x/x_{ref}\right)^{1/2}$$

$x$  and  $y$  are longitudinal and lateral positions leeward of the center of the cylinder. And  $V_0$  and  $D$  are the wind speed and the tower diameter. The tower wake wind speed profile is defined by the 3 parameters: the reference position  $x_{ref}$ , the maximum velocity deficit  $e$  and the width of the tower shadow  $W$  at  $x_{ref}$ . The load equivalent tower shadow model is not defined by the wind speed profile, but by the aerodynamic load history. By the comparison against the CFD results of the rotor-tower configuration.

### 2.3.3 Wind Turbine Outline

The wind turbine investigated here is Fuji Heavy Industries SUBARU 80/2.0, 2 MW prototype downwind turbine. Its and general specifications and outline are shown in Figure 5. The site is located near the seashore in Kamisu, Japan, where the terrain around the turbine is categorized as flat terrain.

### 2.3.4 Simulation Results

The former tower shadow models were defined by wake profiles of isolated tower models. Hereinafter, it is called as ‘‘Isolated Tower Shadow Model’’. The wake profile is determined by any of CFD, wind tunnel test, or field test. CFD around an isolated column was conducted here. Three dimensional CFD was carried out for an isolated column by ANSYS CFX [11] with the SST turbulence model. Figure 6 shows the bell shape tower shadow model defined as Equation (1) (line), which agrees best to the CFD result (circles). Here,  $(e, W, x_{ref}/D)$  was determined as (0.4, 1.3, 5.0).

The proposal here is to define the tower wake profile in BEM to express the load history by CFD of a rotor-tower model. Hereinafter, this is called as ‘‘Load Equivalent Modeling’’, which considers rotor-tower interaction and the transient process of the blades passing through the tower wake. Aerodynamic rotor torque  $M_{XMA}$  and thrust  $F_{XNA}$  at 13 and 25 m/s are shown in Figure 7. The lateral coordinates indicate azimuth angles around the tower shadow. The marks ‘‘o’’ and ‘‘+’’ indicate outputs by rotor tower CFD and BEM, calculated by Bladed [12], with load equivalent model respectively. The bell shape tower shadow model parameters  $(e, W, x_{ref}/D)$  were determined

as (0.08, 5.0, 3.0), on the bases of load equivalence. It expresses the transitions of loads in both wind speeds well, as shown in the figures. BEM results with the former model are also shown in the figures as mark "x". It is remarkable that it provides significantly steeper and narrower load transients. In other words, the former model was shown to overestimate the tower shadow effect, providing larger fatigue loads, and make higher harmonics of vibrations stronger. However, these BEM calculations were carried out with rigid models to coincident with the CFD model, the load equivalent model is applicable to aeroelastic calculation also.



Figure 5 SUBARU 80/2.0 prototype 2 MW downwind turbine

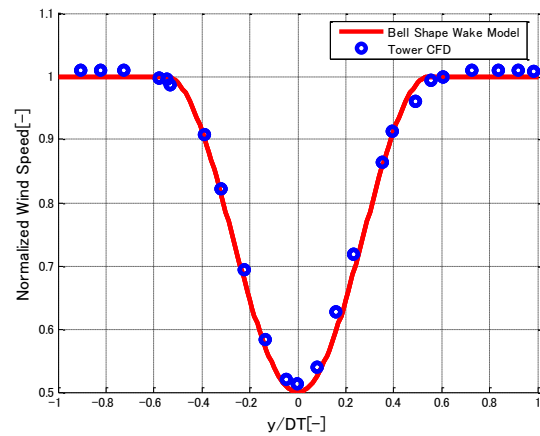


Figure 6 Isolated tower shadow model

### 2.3.5 Validation by the Field Test

The load equivalent model was verified through a field test. The turbine used here was SUBARU 80/2.0, 2MW prototype downwind turbine, explained in the previous section. The main shaft bending moments, calculated by the two tower shadow models, are compared with the field test in Figure 8. The load equivalent model seems to be like the measurement data. On the other hand, the isolated tower wake model tends to overestimate tower shadow effects around 180 degrees azimuth angle.

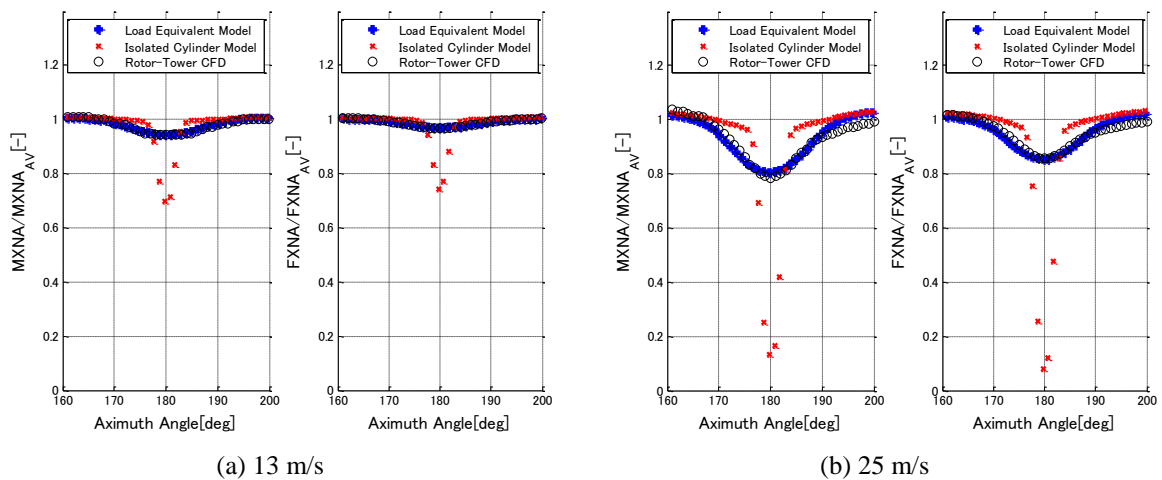


Figure 7 Rotor torque (left) and thrust (right)

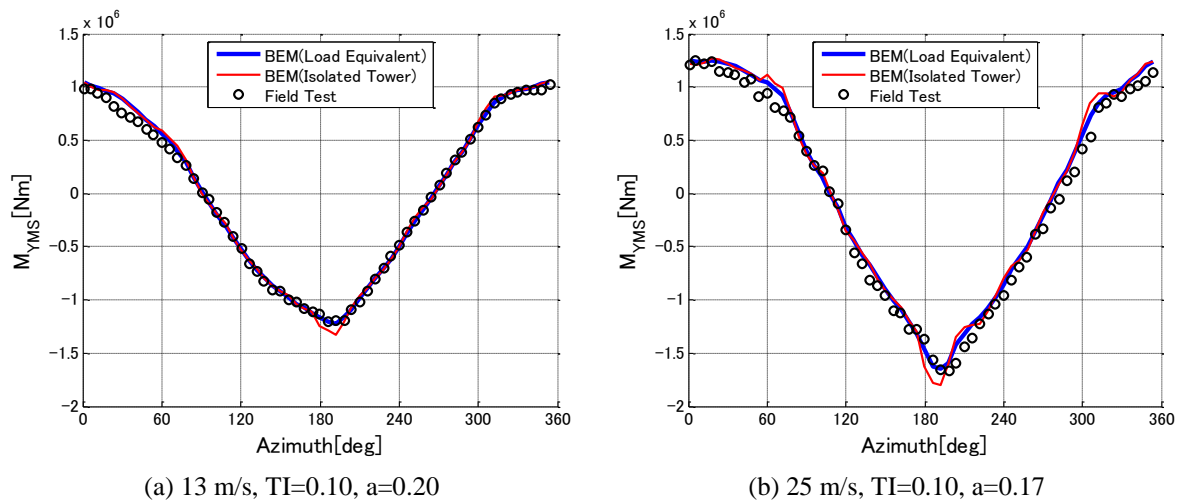


Figure 8 Main shaft bending

### 2.3.6 Summary of the Load Equivalent Tower Shadow Model

Present study proposes the load equivalent tower shadow modeling in BEM aeroelastic simulation method. It defines a bell shape tower wake profile based on equivalence of the load of rotor-tower CFD. It considers rotor-tower interaction and the transition phenomena passing through the tower wake, which has been ignored in former models. The load equivalent tower shadow model was verified by the field test of SUBARU 80/2.0, 2MW downwind turbine.

## 2.4 Dynamic Stall Model for Tower Shadow Effect

### 2.4.1 Background

The load equivalent tower shadow model shown in the previous section does not consider its dynamic effects on the loads. Munduate et al. [24] developed a dynamic stall model for the tower shadow effect. Although it ignores the mutual interaction between the rotor and the tower, it shows good agreement with wind tunnel tests with a 1.0 m rotor diameter, particularly in the context of asymmetry between the entrance and exit of the tower wake. However, the model still demonstrated two problems: (1) it did not express the load increase before the entrance of the tower wake, thereby affecting the fatigue, and (2) it uses an empirical tower wake model to determine the wind speed profile behind the tower. Considering these situations, a dynamic tower shadow modeling method is developed, by modifying and extending Munduate's model to solve problems (1) and (2) mentioned above. Furthermore, the scale effect of the model is also discussed in this study.

This section is based on Yoshida [13].

### 2.4.2 Recommendation

#### (1) For small downwind turbines

The dynamic tower shadow model shown in the present section is recommended for the critical design.

#### (2) For large downwind turbines

The dynamic tower shadow effect can be neglected as shown in the scale effect of the present section.

### 2.4.3 Model Outlines

There are some assumptions in the present methodology. The tower wake is represented by the average wind speed profile with the turbulence ignored, and the trailing vorticity does not affect the lift of the blade element.

The present model is the extension of Munduate et al. [24], aiming for better agreement at the entrance of the wake without using any empirical parameters. The method consists of the following steps:

#### (1) Dynamic Tower Shadow Model

The dynamic tower shadow model is based on Munduate et al. [24]. The deviation of the lift coefficient of the blade section  $\Delta C_l$  while the blade section is passing through the tower wake is

$$\Delta C_l = \frac{2\pi}{W} [w_g(s) - X(s) - Y(s)] \quad (2)$$

where,  $s$  is the normalized time defined as below according to the blade chord length  $c$  and time from the entrance of the tower wake  $t$ .

$$s = \frac{2Wt}{c} \quad (3)$$

and,

$$\begin{cases} X(s) = A_1 \int_0^s \frac{dw_g}{ds} \exp[-b_1(s - \sigma)] d\sigma \\ Y(s) = A_2 \int_0^s \frac{dw_g}{ds} \exp[-b_2(s - \sigma)] d\sigma \end{cases}$$

$$A_1 = A_2 = 0.5, b_1 = 0.13, b_2 = 1.0$$

#### (2) Wind Speed Profile behind the Tower

Moriarty's model, which is used in the aeroelastic simulation code FAST/Aerodyn [18], is applied in this research, among the numbers of models. The formulation of Moriarty's model is as below. The wind speed profiles outside ( $U_{Ex}$ ) and inside of the wake ( $U$ ) at the longitudinal and lateral positions ( $x, y$ ) behind the tower center are provided. Here, the wind speeds are normalized by the free stream wind speed  $U_0$  and the tower radius  $R$ , respectively.  $C_d$  represents the drag coefficient of the tower section.

$$\begin{cases} \frac{U_{Ex}}{U_0} = 1 - \frac{\xi_c^2 - \eta^2}{(\xi_c^2 + \eta^2)^2} + \frac{C_d}{2\pi} \frac{\xi_c}{\xi_c^2 + \eta^2} \dots |\eta| > \sqrt{\delta} \\ \frac{U}{U_0} = \frac{U_{Ex}}{U_0} - \frac{C_d}{\sqrt{\delta}} \cos^2\left(\frac{\pi}{2} \frac{\eta}{\sqrt{\delta}}\right) \dots |\eta| \leq \sqrt{\delta} \end{cases} \quad (4)$$

where,

$$\delta = \sqrt{\xi^2 + \eta^2}, \quad \xi = x/R, \quad \eta = y/R, \quad \xi_c = \xi + 0.01$$

The model expresses the local wind speed increase around the tower and does not contain any empirical parameter, unlike other models.

### (3) Threshold of the Entrance of the Tower Shadow

The entrance of the tower shadow is defined in the present dynamic tower shadow model in the previous section. More practically, it is defined as the initial point of  $s$  in Equation (2), according to Munduate et al. [24], i.e.,

$$\frac{U}{U_0} < 1 \quad (5)$$

The model does not show the load increase around the entrance of the tower wake as mentioned in the previous section, as its wind speed profile does not express the wind speed increase around the tower, as seen in Equation (4). However, the present model can show the wind speed increase around the entrance of the tower wake as Moriarty's model is applied. The following condition is proposed for the tower wake entrance condition in this research, to deal with both the positive and negative deviation with the 1% of dead band:

$$\left| \frac{U}{U_0} - 1 \right| > 0.01 \quad (6)$$

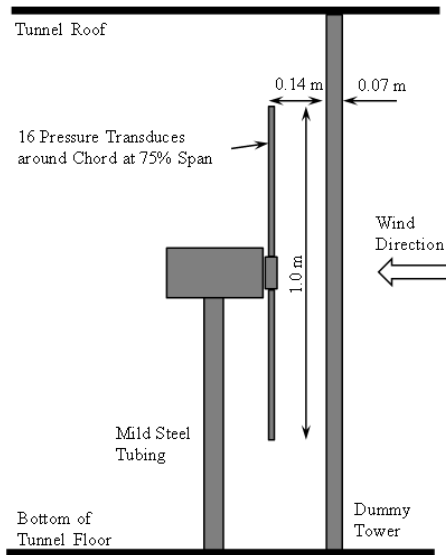


Figure 9 Outline of the wind tunnel test and model setup described in [14].

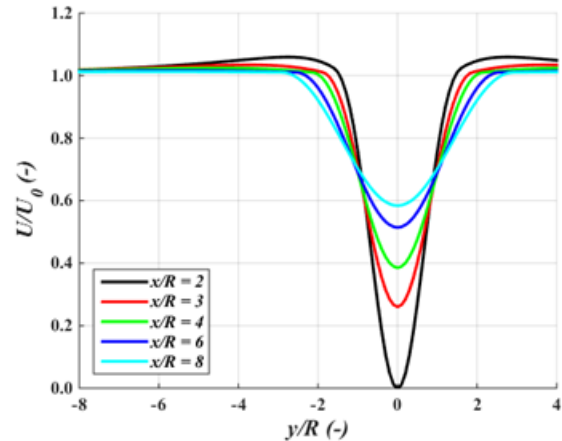


Figure 10 Tower wake wind speed distribution according to Moriarty's model,  $C_d = 1.2$ .

## 2.4.4 Validation of the Model

### (1) Wind tunnel test

The present model was validated with the model and the wind tunnel test data reported by Munduate [14]. The outline of the test is shown in Figure 9. The model has two-bladed rotor with 1.0 m of the rotor diameter. The test was conducted in the Low Speed Wind Tunnel at the University of Glasgow (UG). The variation of the lift coefficient measured by the pressure transducers at 75% rotor radius was used in the experiment. The wind tunnel

test was conducted in three different wind speed 9.0, 11.0 and 11.7 m/s, with the tip speed ratios maintained at 5.34. The tangential speeds at 75% radius are 36.0, 44.1, and 46.7 m/s respectively. The dummy tower, which has 0.07 m of the diameter placed 0.14 m in front of the rotor.

## (2) Wind Speed Distribution

The wind speed distribution calculated in this study is shown in Figure 10. Here, the drag coefficient of the tower section  $C_d$  is assumed to be 1.2, in accordance with the Reynolds number ( $4.5 \times 10^4$ ). It shows narrow and deep distribution, and the local wind speed is higher than the free stream just outside of the tower wake at  $x/R = 2.0$ . It becomes shallower and wider as the wind flows downstream. Here, the rotor position of the test model is at  $x/R = 4.0$ .

## (3) Validation of the Model

Distributions of the deviation of the lift coefficients calculated by the present method by Munduate's and the present thresholds are shown in Figure 11 and Figure 12. Although the overall characteristics such as the depth and the lift drop are almost same, they are slightly different due to differences in the entrance conditions around 160 ~180 degrees.

The deviations of the lift coefficient calculated by the present method with Munduate's threshold are shown in Figure 11. It shows the wind tunnel test ("Experiment UG"), static ("Steady UG") and dynamic ("Unsteady UG") simulation results as seen in [14], as well as the present static ("Steady KU") and dynamic ("Unsteady KU") simulation results. Here, UG and KU stand for University of Glasgow and Kyushu University respectively. The steady data are calculated by  $X = Y = 0$  using Equation (2). Both unsteady methods show much better agreement with the test data compared to the steady data. Although the deviation caused by the differences in the wind speed profiles is small, better agreement is demonstrated by the present method with Munduate's threshold. However, neither of these trials show an increase in lift before it drops at around 160 ~ 180 degrees. In the same manner, the deviations of the lift coefficient calculated in accordance the present method with the present threshold are shown in Figure 12. Unlike Munduate's threshold, it shows a slight increase in lift at the entrance of the tower wake, as does the experiment. However, it is less important than the range from the fatigue and the extreme loads points of view, the recoveries from the lift drop are slower than the experiment. This is considered as the future problem in this research.

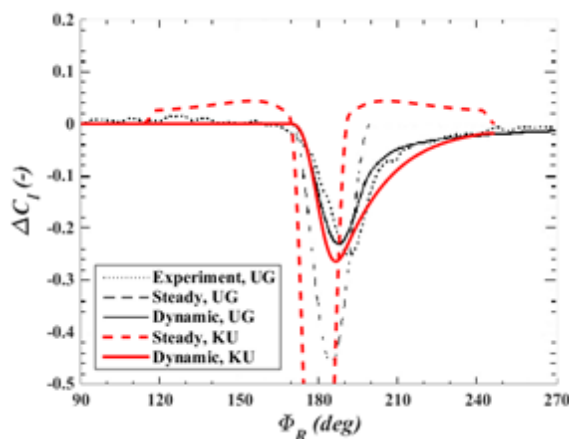


Figure 11 Deviations in the lift coefficient at  $\eta_B = 75\%$  according to the present method with Munduate's threshold,  $C_d = 1.2$ ,  $V_T = 44.1$  m/s.

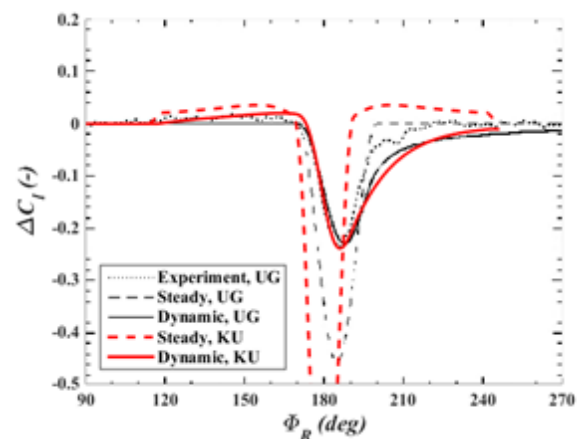


Figure 12 Deviations in the lift coefficient at blade  $\eta_B = 75\%$  according to the present method with the present threshold,  $C_d = 1.2$ ,  $V_T = 36.0$  m/s.

The maximum and the minimum of the three cases are shown in Figure 13. The maximum values by Munduate are zero, as shown above, whereas the present method shows slightly positive values, as does the experiment. The minimum values also show better agreement with the experiment. This difference is quite important, as the range strongly affects the accuracy of the fatigue load.

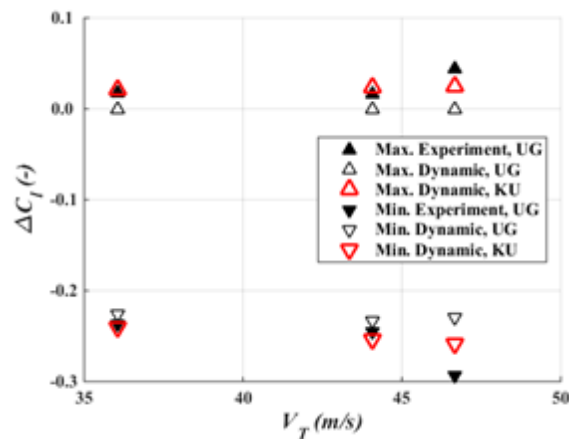


Figure 13 Maximum and minimum deviations in the lift coefficient at  $\eta_B = 75\%$ ,  $C_d = 1.2$ .

#### 2.4.5 Scale Effects

The present method is based on the similarity of the normalized time  $s$  shown in Equation (3). The chord length  $c$  is proportional to the scale of the rotor, whereas the inflow wind speed  $W$  is almost same at the same wind speed and the tip speed ratio. The scale effect of  $s$  is evaluated in this section.

##### (1) Analysis Outline

The wind tunnel test model shown in the previous chapter is herein scaled up to 300% and 1000%. The 100% model is identical to the model presented in the wind tunnel test. Appropriate dimensions of blade, tower, and their relative position is not discussed in this study, assuming their similar configuration. The analysis conditions are wind speed  $U_0 = 9.0$  m/s, and TSR  $\lambda = 5.3$ . In addition, the Reynold number effect on the blade is ignored, as this study focuses on the effect of the blade passing speed.

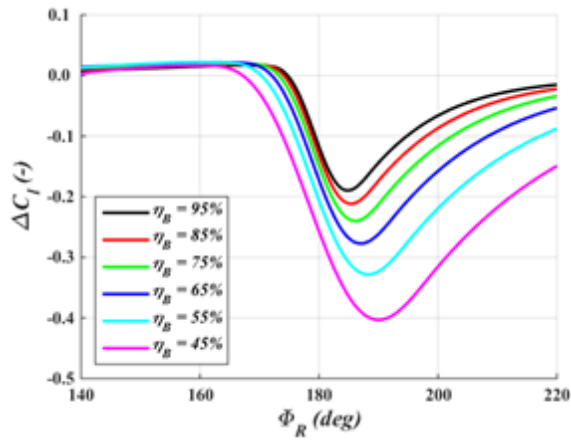
##### (2) Analysis Results

Distributions of wind speed throughout the rotor plane and the deviation of the lift coefficient are shown in Figure 14 for the 300% and the 1000% models at  $C_d = 1.2$ , respectively. Figure 14 (a) shows the same conditions for the 100% model. The deviations of the lift coefficients are completely different, demonstrating that the tower shadow effect becomes much smaller as the blade passing speed increases. The increase in the load around the entrance of the tower shadow also becomes minor.

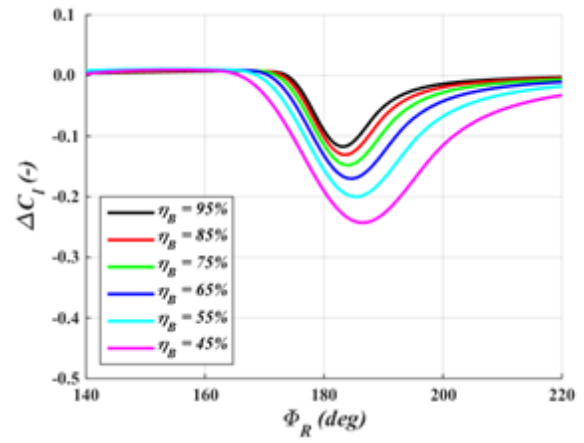
Although these results are dependent on the configurations and operational conditions, the dynamic tower shadow effect generally becomes smaller as the rotor speed decreases.

#### 2.4.6 Summary of the Dynamic Tower Shadow Model

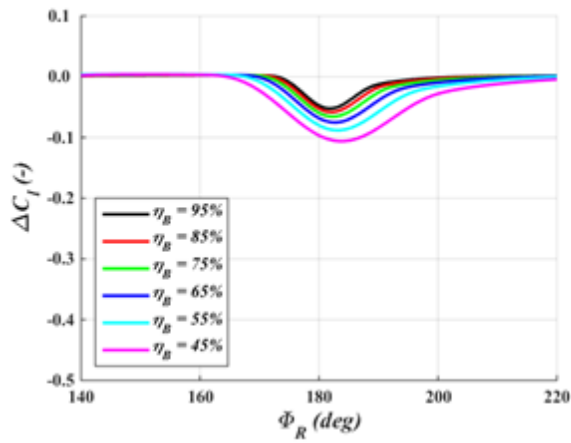
The present research solves the problems dynamic stall in the tower shadow by applying Moriarty's tower wake model and the tower wake entrance conditions obtained from negative wind speed to accept both negative and positive deviations, demonstrating better agreement with the experiment. The present model may be effective in improving the accuracy of the fatigue load analysis, as the range between the maximum and minimum load fluctuations around a tower is vital. The results show that load fluctuation decreases as the scale is increased.



(a) 100% model



(b) 300% model



(c) 1000% model

Figure 14 Deviations in wind speed of the rotor plane and the lift coefficient according to the present method with the present threshold at  $V_T = 36.0$  m/s

## 2.5 Tower Shadow Model for System Engineering

### 2.5.1 Introduction

System engineering approaches are quite essential to evaluate the concept of innovative wind turbines and apply new technologies. Downwind turbine is one of the promising concepts for future economical super-large wind turbines, but no appropriate model for the tower shadow effect had proposed so far. The load equivalent tower shadow model reported in the previous section is too complex for the system engineering, although it is an important design driver. Considering the situations above, a simplified method is proposed in this section. The application of the present model in the system engineering of 10 MW downwind turbine.

This section is based on Namura and Shinozaki [15].

### 2.5.2 Recommendations

The system engineering model for the tower shadow effect of downwind turbines are as shown in the next section.

### 2.5.3 Methodology

#### (1) General

Performance and loads of the wind turbine were evaluated by WISDEM (Wind-Plant Integrated System Design and Engineering Model) [16] developed by National Renewable Energy Laboratory (NREL). WISDEM computes power production, loads, and the cost of wind turbines, according to the blade element momentum (BEM) theory and statistic equations. The loads are calculated as steady state at four rotor azimuth angles (0, 90, 180, and 270 degrees). The power curve is calculated from these loads and rated power of the turbine. Original WISDEM does not consider the tower shadow effects. The tower shadow and the potential flow models are introduced into WISDEM for reasonable LCOE comparison of downwind and upwind turbines from the power production and fatigue damage points of view. Fatigue damage evaluation with the tower shadow and potential flow effects also requires fatigue damage equivalent load (DEL) computation for each design candidate, which has unique design variables such as tower diameter and blade shape, during the optimization process. A simple DEL calculation method based on steady state loads at the four rotor azimuth angles was adopted in this study.

The present method is applied in Section 6 Scaling Benefits of Downwind Turbines.

#### (2) Design Load Cases

WISDEM also evaluates some critical wind conditions for structural constraints. From the experiences in downwind turbine design, prior analyses, and the previous studies, the tower ultimate loads and out-of-plane blade deflection are assumed to occur at IEC design load case (DLC) 1.3, and those for blade occur at DLC 6.1. According to Ning and Petch [17], the load in DLC 1.3 extreme turbulence model (ETM) approximated as  $V_{rated} + 3\sigma_{ETM}$ , where  $V_{rated}$  and  $\sigma_{ETM}$  are the rated wind speed and standard deviation of the wind speed in ETM. The blade bending moment reaches to its maximum when the lift force of the non-rotating blade becomes maximum with the extreme wind model (EWM) at DLC 6.1. The approximation method is introduced to the load definition.

#### (3) Tower Shadow Effect Model

Modified WISDEM considers only steady state three-dimensional wind profiles, including wind shear, tower shadow, and potential flow. The wind shear exponent is 0.11 for EWM and 0.2 for others because cost models for onshore wind turbines are used in this study. No turbulence was introduced to rotor plane.

The wind speed decay induced by the tower shadow was computed by the load equivalent tower shadow model in the section 2.2. In Equation (1), we applied parameter values of Hitachi 2 MW downwind turbines to the present 10 MW turbine optimization. These values were determined to conform the blade load of the BEM analysis with Equation (1) to that of high-fidelity computational fluid dynamics analysis according to the load equivalent tower shadow modeling [10]. For upwind turbines, the potential flow model used in FAST [18] was applied with a tower drag coefficient of 0.5.

#### (4) Power Production Evaluation

Power production is calculated as an inner product of power curve and wind speed histogram following the Rayleigh distribution. Weighted mean of torques generated by a blade at the four rotor azimuth angles (0, 90, 180, and 270 degrees) to properly evaluate power curves affected by the tower shadow and potential flow models. The original WISDEM computed the power curve by simply averaging torques at the four azimuth angles. The equally weighted mean underestimates the power curve because the significantly low torque at the azimuth angle of 180 degrees has quarter contribution. The following equation was used to calculate power equivalent torque  $\bar{Q}$ .

$$\bar{Q} = n_{blade} \left[ \xi Q_{180} + \frac{1-\xi}{3} (Q_0 + Q_{90} + Q_{270}) \right] \quad (7)$$

where  $Q_a$  ( $a = 0, 90, 180, 270$ ) is the torque generated by one blade and computed from the steady state BEM analyses at the azimuth angle of  $a$ ,  $\xi$  is a weight for  $Q_{180}$  which is affected by the tower shadow and potential flow models, and  $n_{blade}$  is the number of blades installed ( $n_{blade} = 3$  in this study).  $\xi$  is determined beforehand to balance wind kinetic energy through the rotor plane (integral of the cube of local wind speed in the rotor plane) computed from the azimuth angles discretized into four and 360. We determined values of  $\xi$  for tower shadow and potential flow models by computing this wind kinetic energy for our wind turbines though suitable  $\xi$  depends on the wind shear exponent, rotor diameter, tower diameter, hub height, etc. In this study,  $\xi = 0.18$  and  $0.15$  were used for tower shadow and potential flow models, respectively. These values should give reasonable approximation of  $\bar{Q}$  for 10 MW turbines.

### 3. TOWER SHADOW MODELS FOR TOWER AERODYNAMIC LOADS

#### 3.1 Information

The tower shadow effect, aerodynamic interaction between the rotor and tower, affects not only for blades but also tower. The tower loads change as rotor thrust changes and as one of the blades approaches and the rotor thrust changes. A steady and a dynamic model of BEM on the tower loads are proposed in this chapter.

#### 3.2 Recommendations

In cases, tower shadow loads on the tower are critical, following models are recommended.

##### (1) Average load

A momentum theory-based model in Section 3.3 is recommended.

##### (2) Dynamic load

A lifting line theory-based model in Section 3.4 is recommended.

#### 3.3 Average Tower Load

##### 3.3.1 Background

The tower of a downwind turbine is in front of the rotor. The wind flow around the towers of downwind turbines, which are located just in front of the rotor, vary by the influence of the rotor thrust. This phenomenon is not modelled in conventional BEM method.

This section proposes a BEM model for the tower average drag based on Yoshida, et al. [19].

##### 3.3.2 Recommendation

The tower average drag coefficient is calculated by the followings.

$$\Delta C_{dT} = \Delta C_{dTv} + \Delta C_{dTP} = -C_{dT0} (1 - \mu_T^2) + \frac{\pi}{2} \mu_T \frac{\partial \mu_T}{\partial \xi_T} \quad (8)$$

where,

$$\xi_T = \frac{x_T}{D_T}$$

$$\mu_T = \frac{u_T}{U_0}$$

By preparing the database of the relationship between the rotor thrust coefficient for the wind speed distribution in front of the rotor, the proposed method is expected to improve the accuracy of the load calculation in the BEM. The relationship between the tower section drag and the rotor thrust, and the virtual tower section is shown in Figure 15.

##### 3.3.3 Methodology

The formulation of the average loads of the towers of the downwind turbine by using the BEM is discussed here. The following two calculations are considered:

##### (1) Wind Speed Distribution by CFD

The wind speed distribution in front of the rotor is calculated using CFD. Figure 16 shows the top view of the rotor and the tower of a downwind turbine. The tower, which has the diameter  $D_T$ , is in front of the rotor. The free stream wind speed  $U_0$  decreases to  $U_0(1 - a)$  at the rotor plane by the rotor thrust. Here,  $a$  is the axial induction factor. Figure 17 is the schematic of the CFD involved in the present study. The tower is not included in the model, but the position is termed “virtual tower position” in this research. Further,  $u_T$  is the wind speed at the virtual tower position, which is between  $U_0$  and  $U_0(1 - a)$ , depending on the condition. The rotor is modeled by an actuator disc

model (ADM).

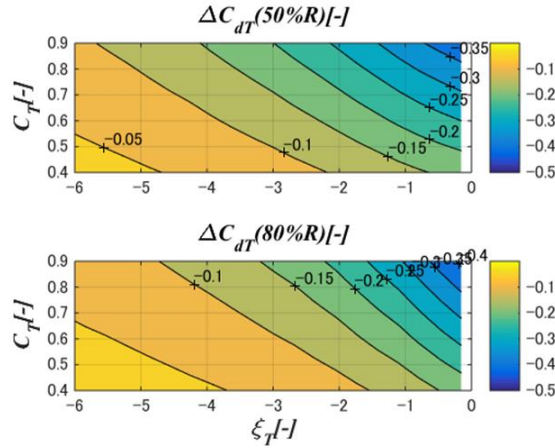


Figure 15 Relationship between the tower section drag and the rotor thrust and the virtual tower position.  $\Delta C_{dT}$ , drag coefficient.

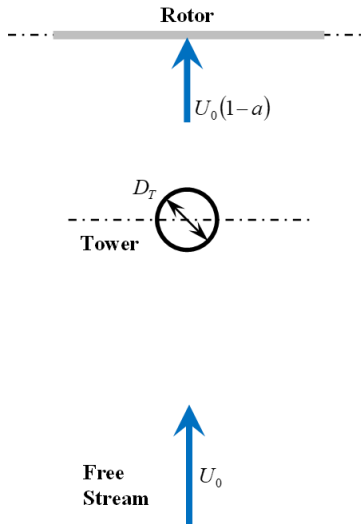


Figure 16 Top view of a downwind turbine.  $U_0$ , free stream wind speed,  $D_T$ , tower diameter.

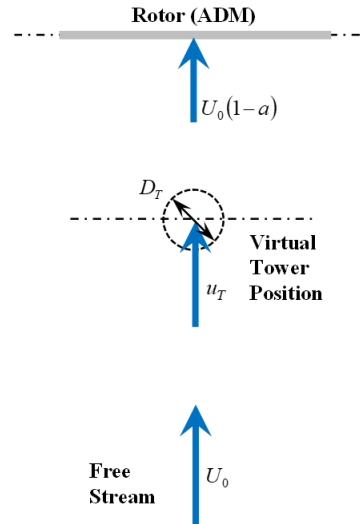


Figure 17 Computational fluid dynamics (CFD) with actuator disc model (ADM).  $u_T$ , wind speed at the virtual tower position.

## (2) Rotor Thrust-Induced Tower Average Drag

The wind speed at the tower and the tower drag decrease as the rotor thrust increases due to the aerodynamic interaction. Two factors, that is, the wind speed and the ambient pressure gradient caused by the rotor thrust, are considered in this research. The formulation assumes the strip theory, according to which the flow between the sections normal to the tower axis is not considered.

### 1) Wind Speed Effect

The tower drag decreases proportionally to the square of the wind speed when the tower section drag coefficient remains constant. This influence is modeled herein.

The section drag  $f_{XT0}$  of the isolated tower with no rotor interaction is as shown in Equation (9):

$$f_{XT0} = \frac{1}{2} \rho U_0^2 D_T C_{dT0} \quad (9)$$

where  $C_{dT0}$  is the drag coefficient at the tower section.

In case the effect of the rotor thrust comes into play, the wind speed at the tower position decreases. Furthermore,

the tower section drag also decreases from  $f_{XT0}$  to  $f_{XT}$ . This is expressed in the following two ways, based on the wind speeds at the free stream and at the virtual tower position, as shown in Equation (10):

$$f_{XT} = \frac{1}{2} \rho U_0^2 D_T C_{dT} = \frac{1}{2} \rho u_T^2 D_T C_{dT0} \quad (10)$$

where  $C_{dT}$  is the tower section drag based on the free stream wind speed, and  $u_T$  is the wind speed at the virtual tower position, which is calculated by CFD without incorporating a tower model, as explained in the previous section. Here, the drag coefficient  $C_{dT0}$  is assumed to be constant as in Equation (9).

Therefore, the tower section drag deviation induced by the rotor thrust  $\Delta f_{XT}$  is calculated as in Equation (11):

$$\Delta f_{XTV} = f_{XT} - f_{XT0} = -\frac{1}{2} \rho U_0^2 D_T C_{dT0} (1 - \mu_T^2) \quad (11)$$

where the normalized wind speed at the virtual tower is  $\mu_T$ .

Therefore, the change in the relevant drag coefficient caused by the wind speed change  $\Delta C_{dT}$  is calculated by Equation (11), as given in Equation (12):

$$\Delta C_{dT} = -C_{dT0} (1 - \mu_T^2) \quad (12)$$

This indicates that the term of the tower section drag decreases as the normalized wind speed at the virtual tower, induced by the rotor thrust, decreases.

## 2) Effect of the Ambient Pressure Gradient

The tower drag is also dependent on the ambient pressure gradient around the tower. This influence is modeled herein. The pressure at the virtual tower position  $p_T$  is calculated by Bernoulli's law. Therefore, the windward pressure gradient  $\partial p_T / \partial x_T$  at the virtual tower center is calculated as shown in Equation (13) by the differential Equation (12):

$$\frac{\partial p_T}{\partial x_T} = -\rho u_T \frac{\partial u_T}{\partial x_T} \quad (13)$$

The section drag by the pressure gradient at the tower section  $\Delta f_{XTP}$  is calculated as in Equation (14) by employing the pressure deviation from the front and back sides of the tower and the tower diameter. The pressure deviation is calculated by the pressure gradient and the windward reference distance:

$$\Delta f_{XTP} = \frac{\partial p_T}{\partial x_T} \Delta x_T D_T \quad (14)$$

Assuming a uniform pressure gradient, the tower section drag is expressed as in Equation (15):

$$\Delta f_{XTP} = \int_{-\pi/2}^{\pi/2} \left( \frac{\partial p_T}{\partial x_T} D_T \cos \phi_T \right) \left( \frac{D_T}{2} \cos \phi_T \right) d\phi_T \quad (15)$$

The reference distance is calculated as in Equation (16) using Equations (14) and (15):

$$\Delta x_T = \frac{\pi}{4} D_T \quad (16)$$

Therefore, the change in the tower section drag owing to the pressure gradient is calculated as in Equation (17):

$$\Delta f_{XTP} = \frac{\pi D_T^2 \rho u_T}{4} \frac{\partial u_T}{\partial x_T} = \frac{\pi D_T \rho U_0^2 \mu_T}{4} \frac{\partial \mu_T}{\partial \xi_T} \quad (17)$$

where  $\xi_T$  is the normalized distance and can be written as

Therefore, the change in the relevant drag coefficient caused by the pressure gradient  $\Delta C_{dTP}$  can be written as in Equation (18):

$$\Delta C_{dTP} = \frac{\pi}{2} \mu_T \frac{\partial \mu_T}{\partial \xi_T} \quad (18)$$

This indicates that the term of the tower section drag decreases as the negative pressure gradient caused by the rotor thrust increases.

### (3) Total Average Tower Drag

From (11) and (17), the deviation of the drag  $\Delta f_{XT}$  and the drag coefficient  $\Delta C_{dT}$  induced by the rotor thrust are derived as Equations (19) and (20), respectively:

$$\Delta f_{XT} = \Delta f_{XTV} + \Delta f_{XTP} = \frac{1}{2} \rho U_0^2 D_T \left[ -C_{dT0} (1 - \mu_T^2) + \frac{\pi}{2} \mu_T \frac{\partial \mu_T}{\partial \xi_T} \right] \quad (19)$$

$$\Delta C_{dT} = \Delta C_{dTV} + \Delta C_{dTP} = -C_{dT0} (1 - \mu_T^2) + \frac{\pi}{2} \mu_T \frac{\partial \mu_T}{\partial \xi_T} \quad (20)$$

### 3.3.4 Wind Tunnel Test

A wind tunnel test for a wind turbine was conducted to validate the theory described in the previous section. The rotor-tower interaction was simulated by a dummy tower placed in front of the rotor of the upwind turbine. The Boundary Layer Wind Tunnel at the Research Institute for Applied Mechanics, Kyushu University, was used for the test. The wind tunnel has a test section with a width of 3.6 m, a height of 2.0 m, and a length of 15 m.

The outline of the two-bladed wind turbine model, with 700 mm of the rotor diameter, is shown in Figure 18. The diameter of the dummy tower is 64 mm, which is 200% the value of the blade chord length. The dummy tower was placed in two positions;  $-6D_T$  and  $-4D_T$ . Rotor speed and the load at the top of the tower, and the pressure on the dummy tower (50%R, 80%R, 8 points each) were measured. Wind speed is 6 m/s, with 4, 6, 8 degrees of blade pitch angle, and 6.6 ~ 9.2 of TSR.

The measurements for the power coefficient  $C_P$  and the thrust coefficient  $C_T$  for the isolated rotor model are shown in Figure 19. The rotor torque was calculated from the rolling moment at the top of the tower. The value of thrust force at the top of the tower was used as the rotor thrust. The maximum value of  $C_P$  was noted at approximately  $\lambda = 8$  and  $\theta = 6$  degrees. However,  $C_T$  tended to increase with an increase in the TSR or a decrease in the pitch angle.

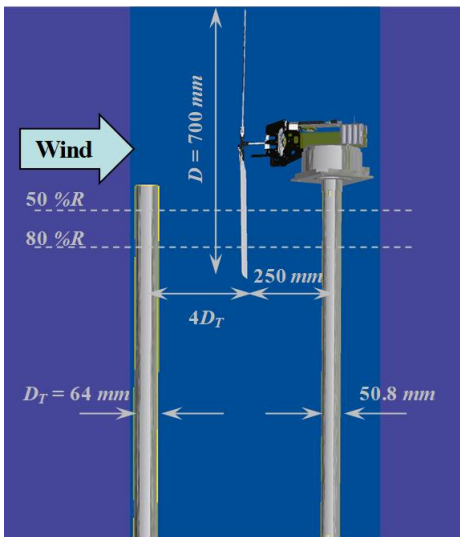


Figure 18 Schematic of the test model (dummy)

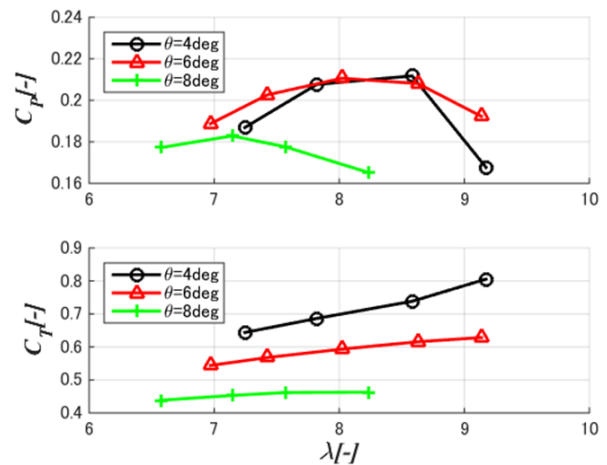


Figure 19 Relationship between the power ( $C_P$ ) and thrust ( $C_T$ ) coefficients and the tip speed ratio.  $\theta$ , blade pitch angle.

tower at  $-4DT$ ).

The pressure distributions on the dummy tower in typical cases are shown in Figure 20. Here, 0 degrees indicate the upwind side of the tower. The pressure on the 50% $R$  was relatively higher than that at 80% $R$ . In general, the pressures around the downwind side of the tower (180 degrees) tended to be higher as the rotor thrust was larger.

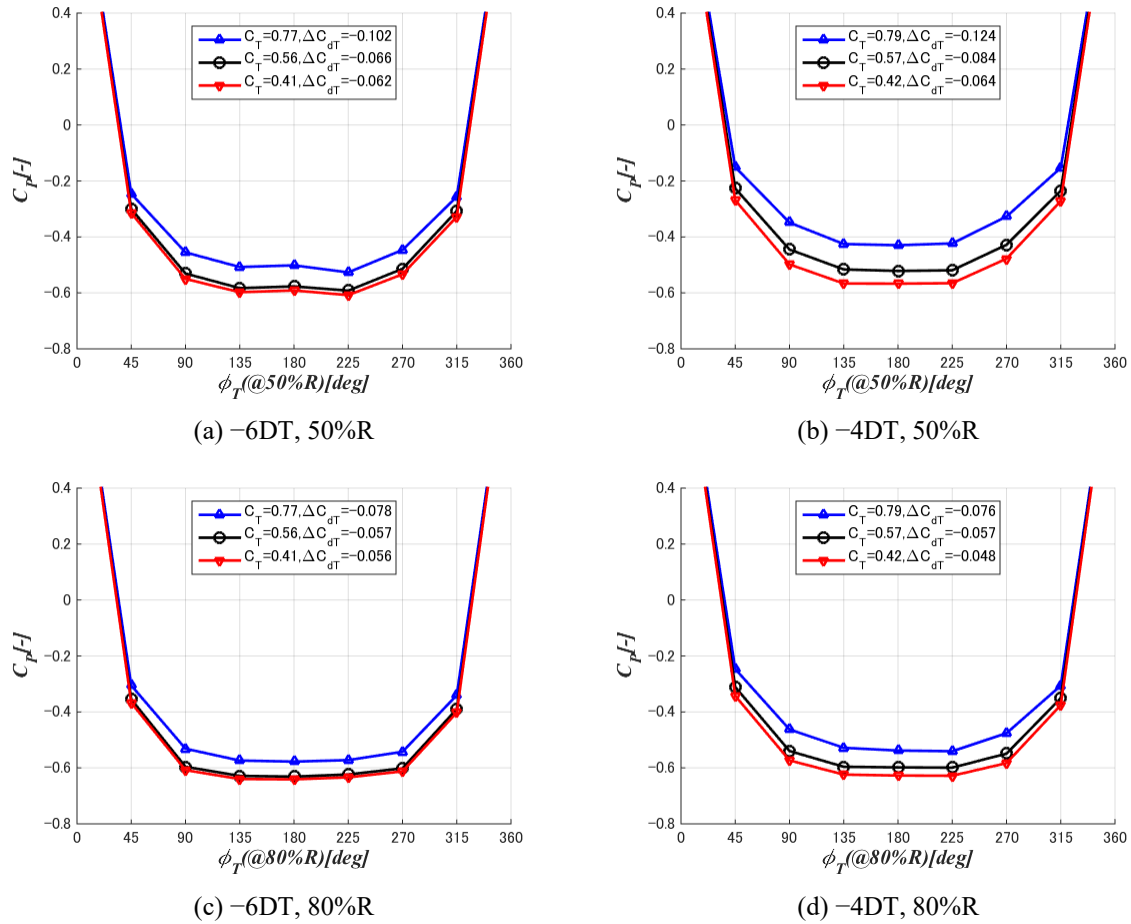


Figure 20 Distribution of the pressure coefficient on the dummy tower in typical cases.

### 3.3.5 Analysis

#### (1) Outline

The relationship between the rotor thrust and the tower drag coefficient was determined by the present method. A CFD analysis was conducted for the rotor using ANSYS CFX [11] considering the  $k-\omega$  SST turbulence model. The rotor was modeled by an ADM with uniform load distribution.

#### (2) Wind Speed Distributions in Front of the Rotor

The wind speed distributions in typical conditions,  $C_T = 0.9$  are shown in Figure 21. The circles in these figures denote the positions of the dummy towers at  $-6DT$  and  $-4DT$ . The wind speed tended to decrease in front of the tower in general, and the wind speed was lower in the vicinity of the rotor. A comparison between the two conditions shows that the wind speed around the dummy tower decreased as  $C_T$  increased. A comparison between the two sections shows that the wind speed in front of the rotor was lower at 50% $R$  compared to that at 80% $R$ . The load was uniform on the rotor, and the inboard sections were considerably affected by the rotor.

The distributions of the normalized wind speed  $\mu_T$  and its differential  $\partial\mu_T/\partial\xi_T$  with respect to the normalized distance  $\xi_T$  in front of the rotor are shown in Figure 22. The distributions at  $C_T = 0.9$  is identical to those in Figure 21 in the symmetrical plane. The top subplots correspond to the distributions at 50% $R$ , and the bottom ones correspond to those at 80% $R$ . The wind speed was lower in the vicinity of the rotor and decreased as the thrust

coefficient increased, as mentioned above.

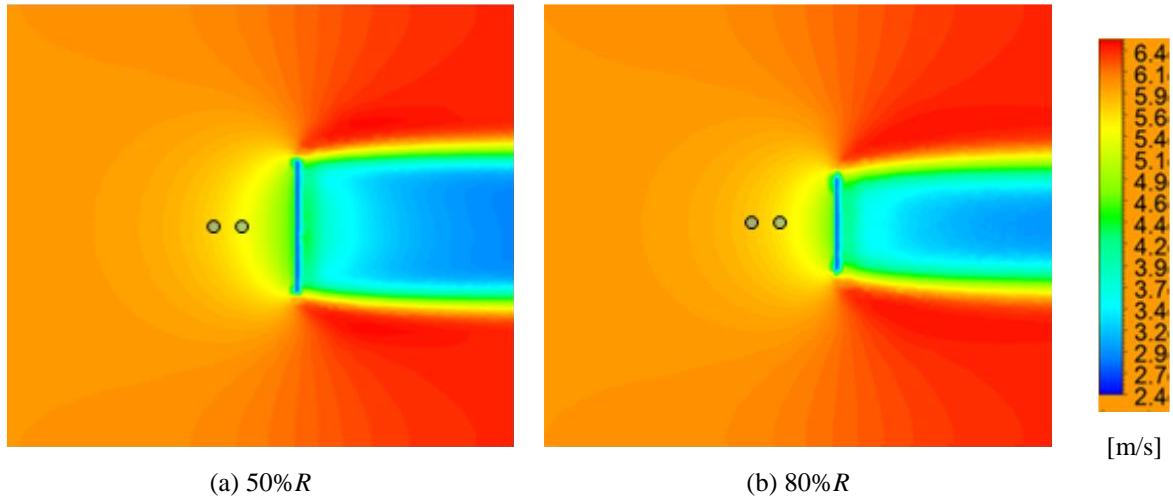


Figure 21 Wind speed distribution in front of the rotor at  $C_T = 0.9$ ,  $U_0 = 6$  m/s. (The circles indicate the dummy tower positions at  $-6D_T$  and  $-4D_T$ ).

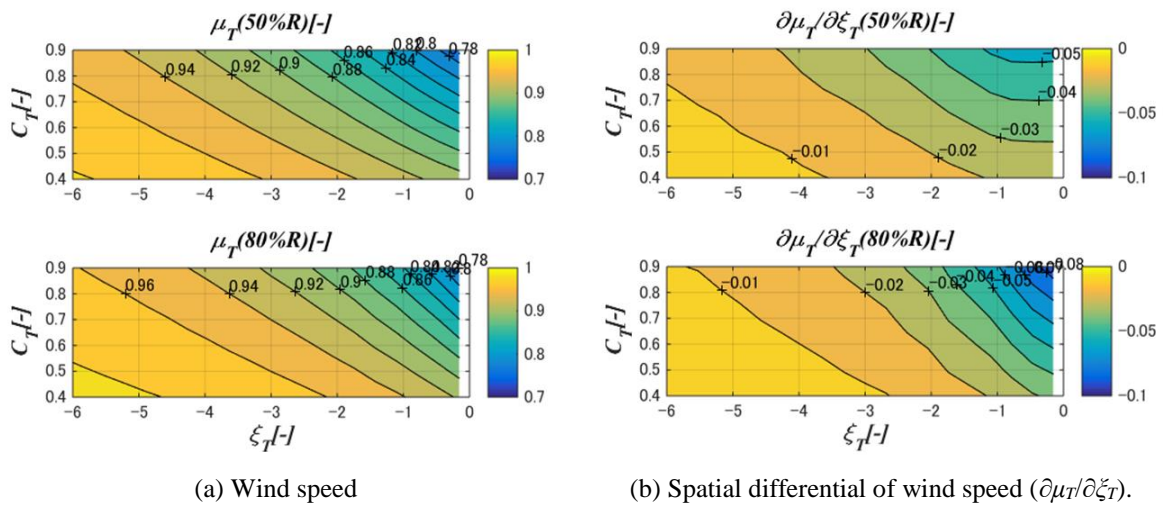


Figure 22 Wind speed and its differential in front of the rotor to thrust coefficient  $C_T$  and normalized distance calculated by CFD (ADM)

### 3.3.6 Validation

The thrust-induced drag deviations  $\Delta C_{dT}$  to the thrust coefficient at  $-6D_T$  and  $-4D_T$  are shown in Figure 23. The lines are linear approximations for which the intercepts are at  $\Delta C_{dT} = 0$  and  $C_T = 0$  by the definition. The  $\Delta C_{dT}$  values for all the cases are shown to be almost proportional to  $C_T$ . The former BEM method does not consider the influence of the rotor thrust on the tower drag. On the other hand, the proposed method shows good agreement with the test. The drag coefficients tended to decrease as the rotor thrust increased. The drag coefficient at the 50%R section was smaller than in the 80%R section. Further, the drag coefficient decreased as the tower was placed closer to the rotor.

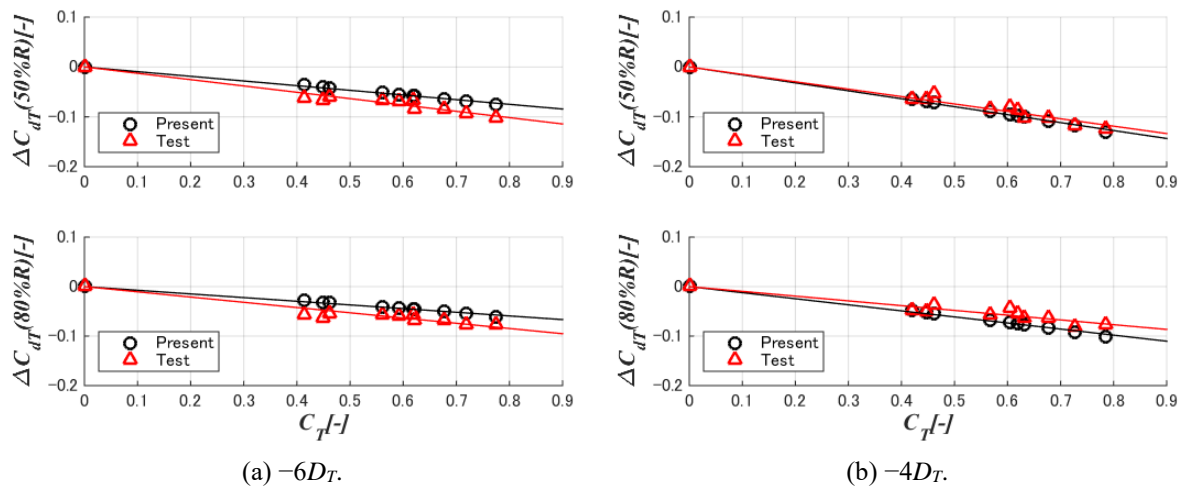


Figure 23 Relationship between tower drag and rotor thrust.

### 3.3.7 Conclusions

A novel analysis method to calculate the average tower drag of downwind turbines, which considers the rotor-induced average tower drag coefficient, was developed. It consists of two terms; 1) the decrease in the wind speed and 2) the pressure gradient caused by the rotor thrust. The rotor thrust distribution is assumed to be uniform. The method was validated by a wind tunnel test. Unlike the former BEM method, which assumes the tower drag to be constant, the proposed method demonstrates a much better agreement with the wind tunnel test, with an accuracy of up to 30%. The results show that the tower drag decreases proportionally to the rotor thrust. Regarding the sensitivity of the tower drag with respect to the rotor thrust, the following characteristics were noted:

- The drag coefficient was larger in the inboard section (50% $R$ ) than in the outboard section (80% $R$ ).
- The drag coefficient decreased as the tower was positioned closer to the rotor.
- Of the two terms influencing the deviation of the tower section drag, the effect of the decrease in wind speed was more dominant in leading to the decrease in the tower section drag.

### 3.4 Dynamic Tower Load

#### 3.4.1 Background and Objectives

The rotor tower interaction of tower shadow effect affects tower dynamic loads. However, there was no appropriate model had not reported to this point. Considering these situations, a dynamic tower shadow modeling method was developed for the BEM calculation of downwind turbines using the lifting line (LL) theory.

This section is based on Yoshida [20].

#### 3.4.2 Recommendation

In cases, the aerodynamic interaction is strong and the influence on the tower load is critical, the tower section drag coefficient is calculated as below.

$$\Delta C_{dT} = \frac{df_{xT}/dz_T}{\rho U_0^2 D_T/2} = \frac{\pi D_T}{2U_0^2} \left( -U_0 \frac{du}{dx_T} + r\Omega \frac{dv}{dx_T} - w \frac{dw}{dx_T} \right) \quad (21)$$

where,

$$\frac{d\mathbf{u}}{dx_T} = \sum_{n=1}^B \left( \int_0^R \frac{\Gamma}{4\pi} \mathbf{e}_{BZ} \times \frac{d}{dx_T} \left( \frac{\mathbf{e}_{TB}}{\Delta x_{TB}^2} \right) dr \right)_n$$

#### 3.4.3 Methodology

The present method consists of the following four steps.

##### (1) Rotor BEM

The present model is aimed for application for blade-element and momentum (BEM) method, which is the most common theory for the wind turbine load calculation due to its productivity and accuracy.

##### (2) Blade Circulation

The circulation of the blade sections is calculated by the lifting line theory as Equation (22).

$$\Gamma = \frac{1}{2} W c C_l \quad (22)$$

##### (3) Blade-Induced Wind Speed and Pressure around Tower

The velocity  $du$  induced by the circulation  $\Gamma$  of the blade section  $dr$  in the previous section is calculated by the Biot-Savart law in Equation (23).

$$d\mathbf{u} = \frac{\Gamma}{4\pi} \frac{\mathbf{e}_{BZ} \times \mathbf{e}_{TB}}{\Delta x_{TB}^2} dr \quad (23)$$

where  $e_{BZ}$  is the unit vector along the blade axis, and  $\Delta x_{TB}$  is the vector from the blade section to the tower section, which consists of the distance  $\Delta x_{TB}$  and the unit vector  $e_{TB}$  in Equation (24).

$$\Delta \mathbf{x}_{TB} = \mathbf{e}_{TB} \Delta x_{TB} \quad (24)$$

The schematic of the equation is shown in Figure 24. Here,  $du$  is normal to both of  $e_{BZ}$  and  $e_{TB}$ .

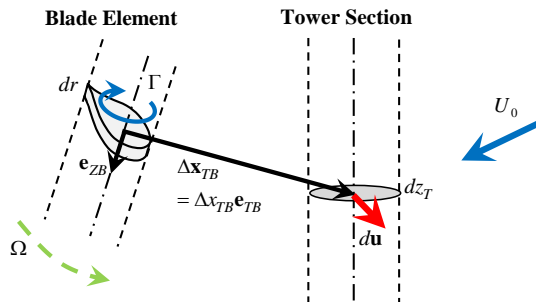


Figure 24 Schematic of the induced velocity  $du$  at the tower element  $dz_T$ , induced by the circulation  $\Gamma$  at the

blade element  $dr$ .

Therefore, the total induced velocity  $u$  on the tower axis is calculated in Equation (25) by integrating along all the blades.

$$\mathbf{u} = \sum_{n=1}^B \left( \int_0^R \frac{\Gamma}{4\pi} \frac{\mathbf{e}_{BZ} \times \mathbf{e}_{TB}}{\Delta x_{TB}^2} dr \right)_n \quad (25)$$

The derivative to the windward, or tower  $x_T$  axis, is defined in Equation (26).

$$\frac{d\mathbf{u}}{dx_T} = \sum_{n=1}^B \left( \int_0^R \frac{\Gamma}{4\pi} \mathbf{e}_{BZ} \times \frac{d}{dx_T} \left( \frac{\mathbf{e}_{TB}}{\Delta x_{TB}^2} \right) dr \right)_n \quad (26)$$

where  $R$  is the rotor radius.

The pressures at the locations of the tower center are calculated by Bernoulli's law. The pressure deviation  $p_T$  between the conditions with and without blade circulation is approximated as Equation (27) assuming  $a_T \ll 1$  and  $a_T' \ll 1$ .

$$\begin{aligned} p_T &= p_{T1} - p_{T0} \\ &= -\rho u U_0 (1 - a_T) + \rho v r \Omega (1 + a_T') - \frac{1}{2} \rho w^2 \\ &\approx -\rho u U_0 + \rho v r \Omega - \frac{1}{2} \rho w^2 \end{aligned} \quad (27)$$

Therefore, the pressure differential  $dp_T/dx_T$  is shown in Equation (28).

$$\frac{dp_T}{dx_T} = -\rho U_0 \frac{du}{dx_T} + \rho r \Omega \frac{dv}{dx_T} - \rho w \frac{dw}{dx_T} \quad (28)$$

#### (4) Tower Section Drag Variation by Blade Induction

The drag per unit length on the tower section  $df_{xT}/dz_T$  is calculated from Equation (29), assuming a uniform pressure for the reference distance  $\Delta x_T$  around the tower section.

$$\frac{df_{xT}}{dz_T} = D_T \frac{dp_T}{dx_T} \Delta x_T \quad (29)$$

Assuming the uniform pressure slope above,  $df_{xT}/dz_T$  is also expressed in Equation (30) more generally.

$$\frac{df_{xT}}{dz_T} = \int_{-\pi/2}^{\pi/2} \left( \frac{dp_T}{dx_T} D_T \cos \phi_T \right) \left( \frac{D_T}{2} \cos \phi_T \right) d\phi_T \quad (30)$$

The reference distance is calculated in Equation (31) from Equations (29) and (30).

$$\Delta x_T = \frac{\pi}{4} D_T \quad (31)$$

Therefore, the tower section load deviation from the rotor interaction is shown in Equation (32)

$$\frac{df_{xT}}{dz_T} = \frac{\pi \rho D_T^2}{4} \left( -U_0 \frac{du}{dx_T} + r \Omega \frac{dv}{dx_T} - w \frac{dw}{dx_T} \right) \quad (32)$$

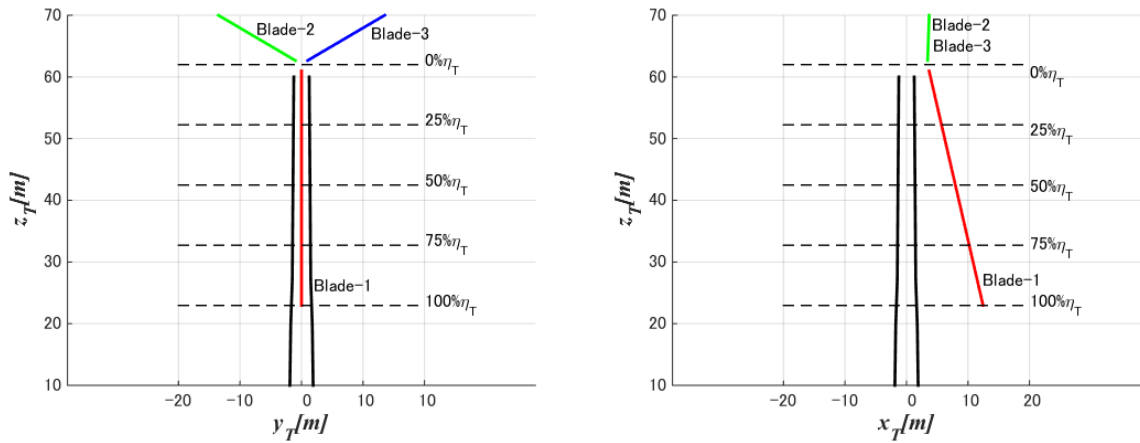
Furthermore, the deviation of the tower section drag coefficient  $\Delta C_{dT}$  is shown in Equation (33).

$$\Delta C_{dT} = \frac{df_{xT}/dz_T}{\rho U_0^2 D_T/2} = \frac{\pi D_T}{2U_0^2} \left( -U_0 \frac{du}{dx_T} + r\Omega \frac{dv}{dx_T} - w \frac{dw}{dx_T} \right) \quad (33)$$

3.4.4 Analysis Conditions

The prototype of the SUBARU 80/2.0 downwind turbine (Figure 5, Figure 25) [9,10] is used in this study. It is the first MW-class commercial downwind turbine, which has 80 m the of rotor diameter and 2.0 MW of the rated power. The schematics of the rear view ( $-x_T$ ) and the side view ( $+y_T$ ) are calculated as shown in Figure 26, assuming a rigid structure. The rotor rotates counterclockwise in the rear view. The five lines in these figures show the tower stations  $\eta_T$  in front of the blade station radius  $r$  normalized by the rotor radius  $R$  at 180 degrees from the rotor azimuth angle. A large clearance is maintained by the tilt and coning of the rotor.

The distributions of the blade chord length  $c$ , the tower diameter  $D_T$ , and their ratio are shown in Figure 27. Bladed [12] is used for the BEM, and the model is assumed to be stiff. The normalized clearance between the tower and the rotor  $\Delta x_R/D_T$  at 6 degrees (rated, 13 m/s) and 26 degrees (cut-out, 25 m/s) of blade pitch angles, rotor speeds are  $17.5 \text{ min}^{-1}$  in both cases.



(a) Rear view ( $-x_T$ ) of the wind turbine. (b) Side view ( $+y_T$ ) of the wind turbine.

Figure 25 Schematic of the wind turbine at 180 degrees of the rotor azimuth angle.

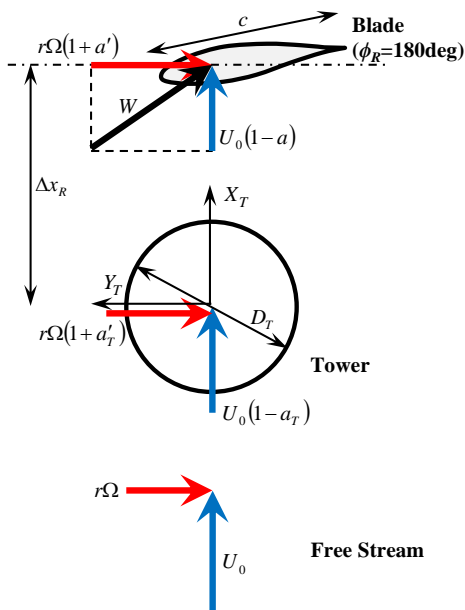


Figure 26 Relative wind speeds at the blade section (180 degrees of azimuth angle), tower section, and free stream.

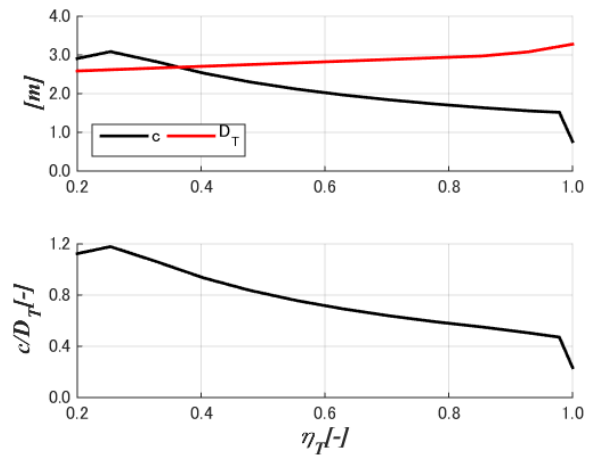


Figure 27 Blade chord length  $c$ , tower diameter  $D_T$ , and their ratio  $c/D_T$

### 3.4.5 Analysis Results

#### (1) Rotor BEM

The distributions of the lift coefficient  $C_l$  and circulation  $\Gamma$  along the blade are shown in Figure 28. The distribution of the  $\Gamma$  is like the  $C_l$ , as the relative wind speed and chord length are proportional and inversely proportional to the blade station radius, respectively. The out-of-plane load  $dF_{XB}/dr$  and the in-plane load  $dF_{YB}/dr$  are shown in Figure 29.

#### (2) Blade Circulation

The distributions of the circulations are shown in the bottom subplot in Figure 28. Although the distribution is almost uniform at 13 m/s, it is quite smaller in the outboard section at 25 m/s.

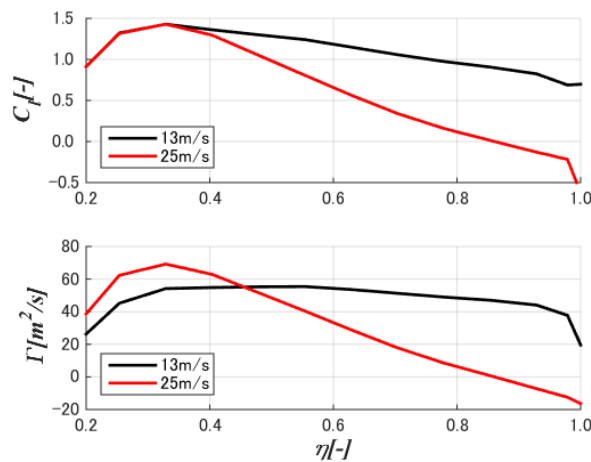


Figure 28 Lift coefficient  $C_l$  and circulation  $\Gamma$  along the blade.

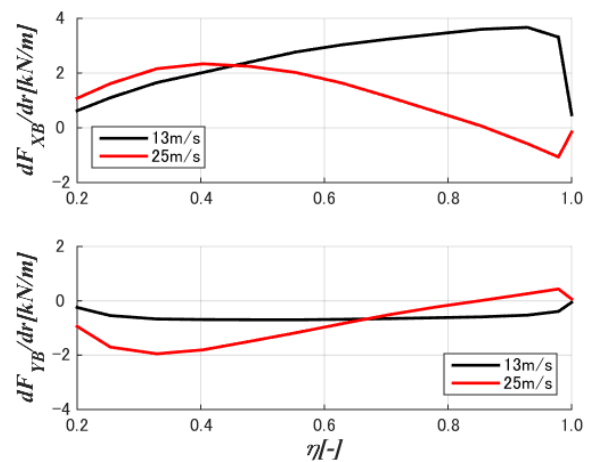


Figure 29 Axial and tangential blade aerodynamic loads  $F_{XB}$  and  $F_{YB}$  per unit length.

#### (3) Blade Induced Wind Speed and Pressure around the Tower

The induced velocity of the total of three blades and blade 1 is shown in Figure 30, where  $\phi_R$  is the rotor azimuth angle, which is same as for blade 1. The top and bottom subplots show the axial and tangential velocities at the tower center. The axial velocity changes from positive to negative at 180 degrees of rotor azimuth. The tangential velocity takes on a maximum value here. The interactions of the blades are most distinct around 180 degrees and are mainly caused by the closest blade. However, the neighboring blades are affected slightly at approximately 120 and 240 degrees but negligibly at approximately 180 degrees.

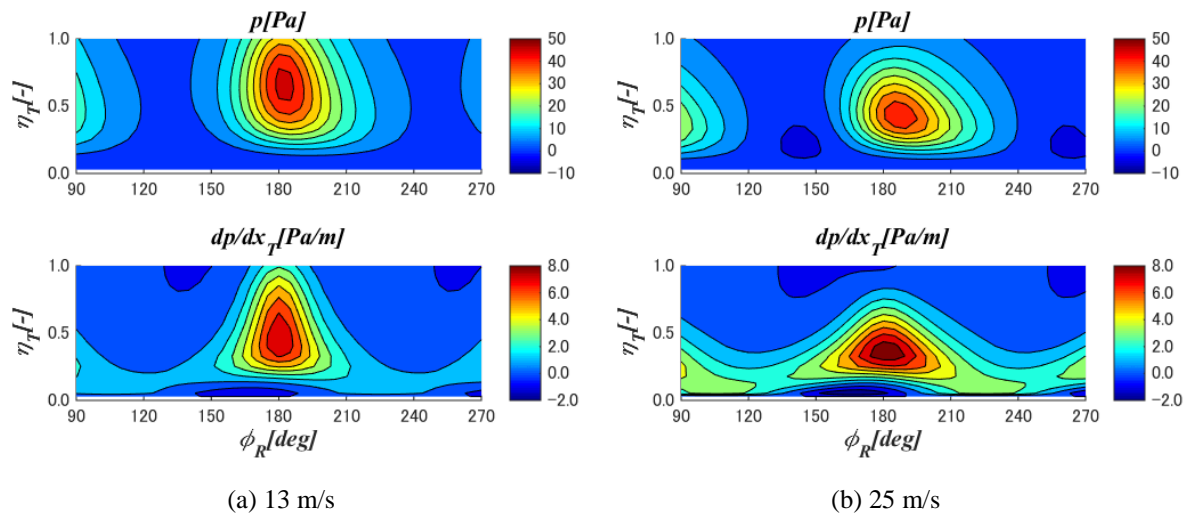


Figure 30 Induced pressure and pressure gradients at the tower with respect to the rotor azimuth  $\phi_R$  and the tower

section  $\eta_T$ .

#### (4) Tower Section Drag Variation by Rotor Induction

The deviations of the tower drag and its coefficients with respect to the tower section and the rotor azimuth angle are shown in Figure 31. The deviations of approximately 180 degrees of the azimuth angle at 13 m/s show steeper characteristics than at 25 m/s. Obviously, the deviations at 13 m/s are much larger than at 25 m/s. In other words, the deviations in the tower loads from the tower shadow effect are small at 25 m/s.

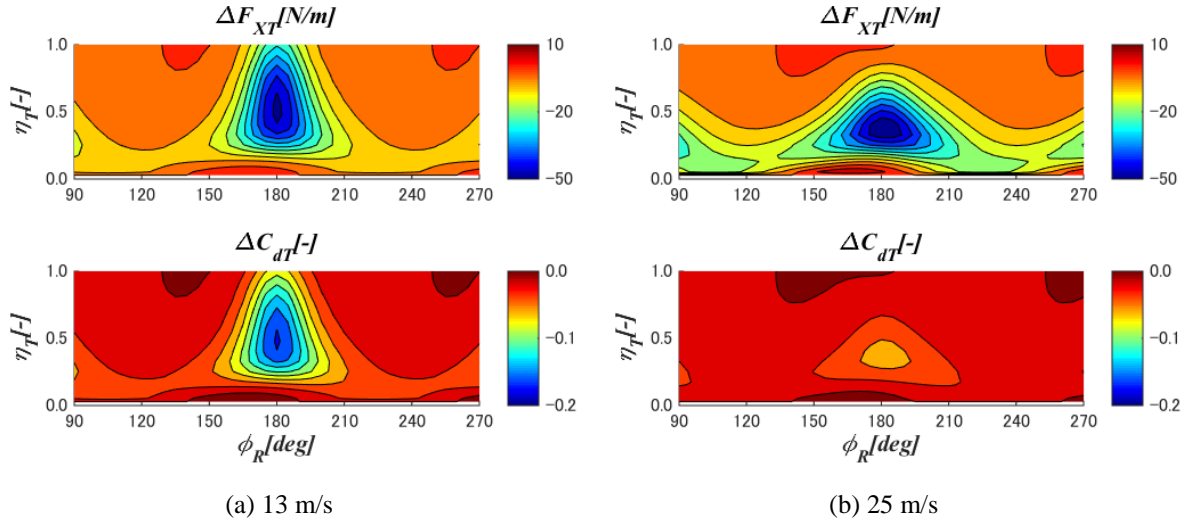


Figure 31 Induced drag and drag coefficients of the tower sections with respect to the rotor azimuth  $\phi_R$  and the tower section  $\eta_T$ .

### 3.4.6 Verification by CFD

#### (1) CFD Outlines

The results in the section chapter are verified by CFD in reference [9]. The ANSYS CFX [11] with  $k-\omega$  SST turbulence model is used with the sliding mesh model for coupling of the rotating rotor and the fixed tower. The two simulation conditions, rated (13 m/s) and cut-out (25 m/s) wind speeds, are identical as in the previous section.

#### (2) Verification Tower Variable Loads

Variations of the drag coefficients  $\Delta C_{dT}$  and the deviation from the average of 4 typical tower sections  $\eta_T$  at 13 m/s and 25 m/s are shown in Figure 32. Here, “BEM+LL” indicates the present method and “BEM (Conv)” is the conventional BEM, which considers the constant tower drag coefficient for the tower aerodynamics.

The  $\Delta C_{dT}$  at 100%  $\eta_T$  are shown in Figure 32(a). The top and bottom subplots show 13 m/s and 25 m/s, respectively. The variations are almost zero for all three cases at 25 m/s, where the circulations of the blade outboard sections are around zero, as shown in Figure 28. However, the differences at 13 m/s are distinct. The present method shows almost identical variations with the CFD in both the amplitude and phase, which is different from the conventional method. This indicates that the present model does not express the load variations in cases where the circulation is large.

The  $\Delta C_{dT}$  at 75% and 50%  $\eta_T$  in Figure 32(b), (c) are also like Figure 32(a). The variation in the present method is in good agreement with the CFD at 13 m/s, although the deviations from the CFD are larger than for the 100%  $\eta_T$ . This is still obviously better than for the conventional BEM, which shows a constant value.

One of the factors is the effect of the tower wake on the blade load, which is neglected in the present model. The rotor-tower clearance (Figure 6) gets smaller inboard and is smaller than  $2.5 D_T$  and  $2.0 D_T$  from the center and the surface of the tower between 20~40%  $\eta_T$ . The blade chord length to tower diameter ratio (Figure 27) is larger than 0.8 between 20~50%  $\eta_T$ . Both of the two conditions above decrease the accuracy of the present model.

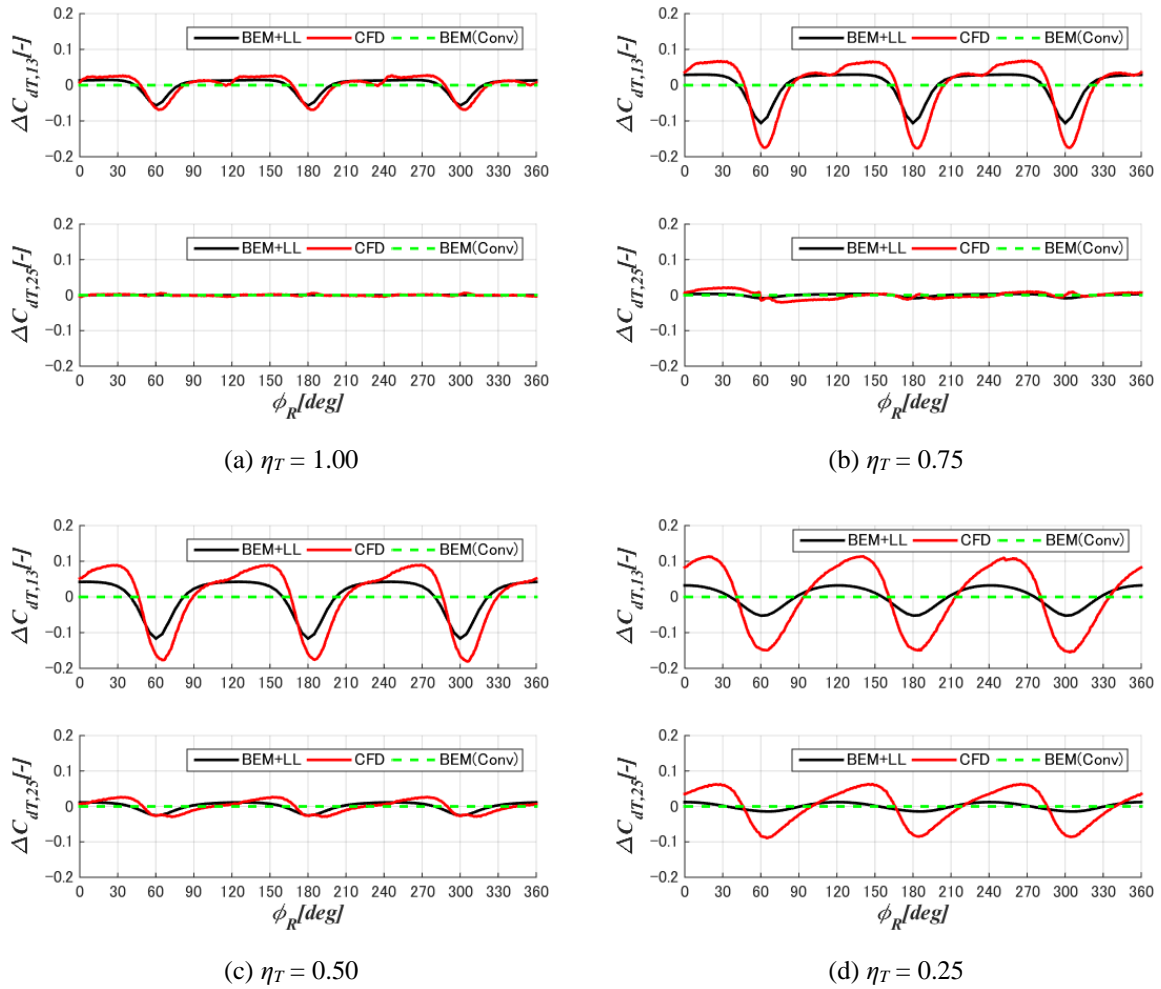


Figure 32 Tower section drag coefficients  $\Delta C_{dT}$  as to the rotor azimuth  $\phi_R$ .

### 3.4.7 Conclusions

The lifting line model-based blade interaction method to determine the tower load via the blade-element and momentum method is formulated in this study. The model expresses the load variations, which were neglected in former models. The method indicates that most of the interaction is provided by the closest blade, especially in the vicinity of the tower section. Additionally, the effect of the lateral induction is much larger than the axial and vertical effects. The method was verified with CFD for a 2 MW, 3-bladed downwind turbine.

The tower load variations according to the present model in outboard sections, where the rotor-tower clearance is large ( $>3.0$  times of the tower diameter) and the ratio of the blade chord length is small ( $<0.5$  times of the tower diameter), are shown to be accurate in both rated and cut-out conditions. The present model expresses the amplitude and phase of the tower load variation in different thrust conditions in outboard sections.

There is room for improvement in inboard sections, where the rotor-tower clearance is small and the blade chord to the tower diameter is large. Furthermore, the model is planned to be extended to blade load deviation in a future study.

## 4. NACELLE BLOCKAGE EFFECT

### 4.1 Introduction

With respect to the three-dimensional effects in the blade-element and momentum (BEM) method, the tip/root effect is one of the most essential considerations because of the edges at the blade tip and root. Although only “loss” has been focused on the root effect, downwind rotors are expected to have a stronger blockage effect, that is an aerodynamic interaction with the nacelle. The nacelle blockage effects on the rotor performance and loads were modeled and verified numerically.

This chapter is based on Anderson, et al. [21].

### 4.2 Recommendation

The nacelle blockage effect model is recommended to consider for the load calculation in cases of the nacelle or the spinner is large. Otherwise, its effect is negligible.

Consider the wind speed distribution induced by the nacelle by CFD or experiment. In cases of the BEM with the wind speed distribution in the rotor plane is determined by simulations or experiments. In cases of the elliptic nacelle, the following model introduced by the potential model is applicable.

$$\phi = A\mu \left[ \frac{1}{2}\zeta \log \frac{\zeta + 1}{\zeta - 1} - 1 \right], \quad \text{with} \quad A = U_0 a \left[ \frac{1}{1 - e^2} - \frac{1}{2e} \log \frac{1 + e}{1 - e} \right]^{-1} \quad (34)$$

$$\mu = \frac{x}{k\zeta}, \quad \zeta = \frac{\sqrt{-B + \sqrt{\Delta}}}{\sqrt{2}k}, \quad \text{with} \quad B = -(k^2 + x^2 + r^2), \quad \Delta = B^2 - 4k^2x^2 \quad (35)$$

$$u_x = \frac{\partial\phi}{\partial x} = \frac{\partial\phi}{\partial\mu} \frac{\partial\mu}{\partial x} + \frac{\partial\phi}{\partial\zeta} \frac{\partial\zeta}{\partial x} \quad u_r = \frac{\partial\phi}{\partial r} = \frac{\partial\phi}{\partial\mu} \frac{\partial\mu}{\partial r} + \frac{\partial\phi}{\partial\zeta} \frac{\partial\zeta}{\partial r} \quad (36)$$

where,

$$\begin{aligned} \frac{\partial\phi}{\partial\mu} &= \frac{\phi}{\mu} & \frac{\partial\mu}{\partial x} &= -\frac{x}{k\zeta^2} \frac{\partial\zeta}{\partial x} + \frac{1}{k\zeta} & \frac{\partial\mu}{\partial r} &= -\frac{x}{k\zeta^2} \frac{\partial\zeta}{\partial r} \\ \frac{\partial\phi}{\partial\zeta} &= \mu \frac{A}{2} \left[ \log \frac{\zeta + 1}{\zeta - 1} - \frac{2\zeta}{\zeta^2 - 1} \right] & \frac{\partial\zeta}{\partial x} &= \frac{x}{\sqrt{\Delta}} \left[ \zeta - \frac{1}{\zeta} \right] & \frac{\partial\zeta}{\partial r} &= \frac{r\zeta}{\sqrt{\Delta}} \end{aligned}$$

### 4.3 CFD Outlines

To evaluate the present method, CFD was conducted for typical nacelle shapes shown in Figure 33 and Table 3. Here, “EM” indicates the engineering model defined in this section.

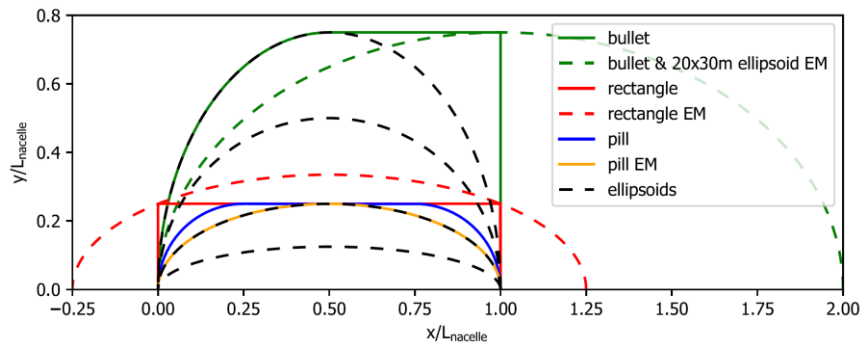


Figure 33 CFD cases

Table 3 CFD Parameters verified

Suite	Objective	Parameters Varied
1	Determine if root airfoils respond to nacelle blockage effects	Root airfoils
2	Determine blockage effects of different nacelle geometries	Nacelle shape (ellipsoid, pill, and rectangle)
3	Determine blockage effects of different nacelle aspect ratios	Nacelle height [5, 10, 20, 30] m
4	Determine relationship between Re and blockage effects	Inflow velocity [3, 15, 25] m/s
5	Compare CFD models; determine blockage effect of TI	CFD method (body-force/geometry-resolved), TI

#### 4.4 CFD Results

The wind speed distributions of typical configurations, 20 m x 30 m bullet and ellipsoid, calculated by CFD are shown in Figure 34. The latter is the EM configuration of the former one. They show similar distributions in the upwind and the middle of the bodies.

The CFD results for the three nacelle shapes with the three rotor planes are shown in Figure 35. The lines from left to right, are upwind, middle, and downwind respectively. Note: the rectangle EM is wider in the middle.

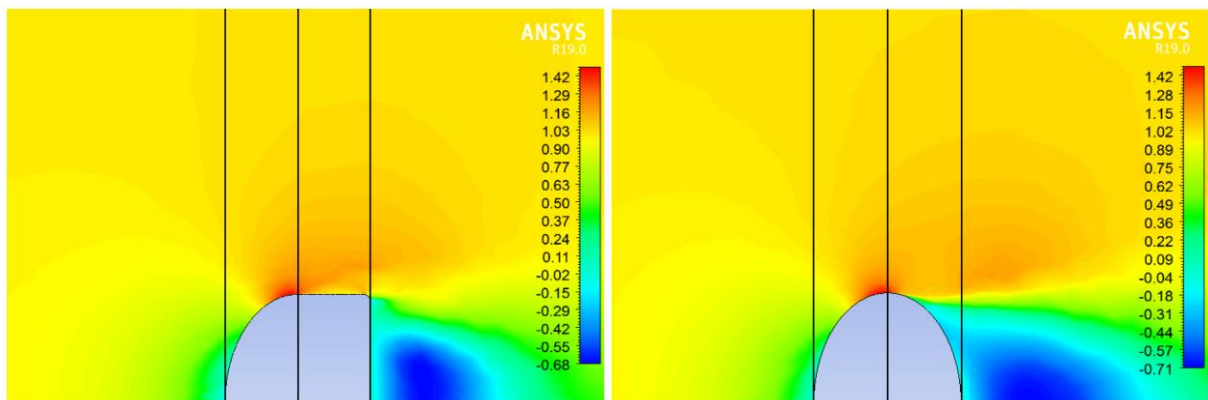
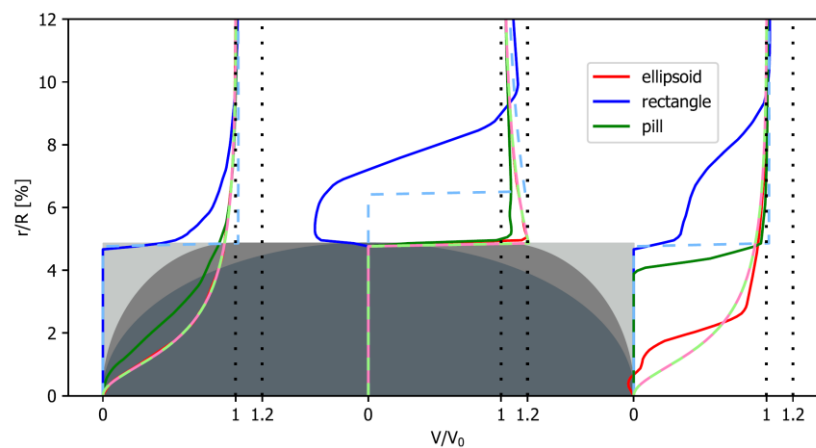
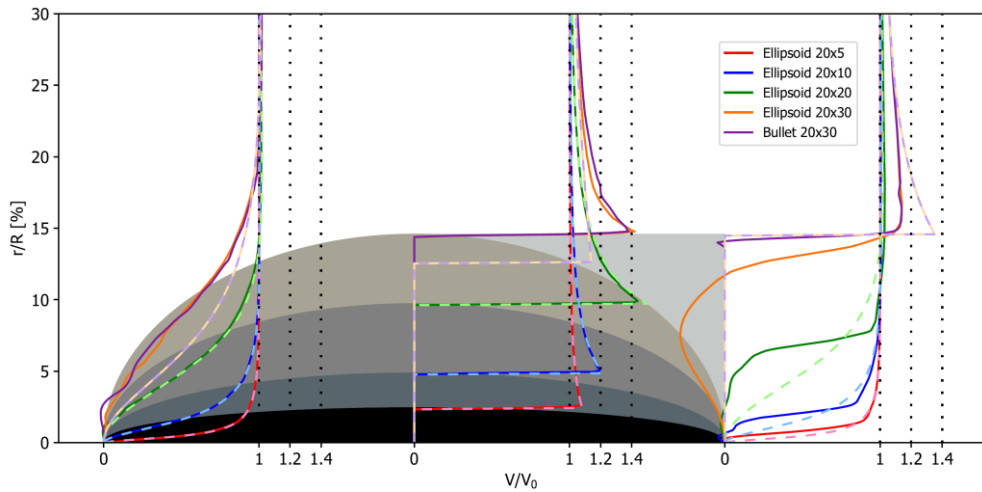


Figure 34 Normalized velocities by CFD around the 20 m x 30 m bullet (left) and ellipsoid (right) nacelles.



(a) Various nacelle shapes.



(b) Various nacelle heights of ellipsoid.

Figure 35 Normalized velocities profiles along rotor planes.

Solid, darker lines: CFD results. Dashed, lighter lines: EM results.

The relationship between boundary layer height  $BLH$  from CFD, and Reynolds numbers  $Re_L$ ,  $Re_H$ , and aspect ratio of all the nacelles are shown in Figure 36. No correlation is found between  $BLH$  and  $Re$ , though an inverse relationship is found between  $BLH$  and aspect ratio. No correlation is found between maximum speed up and  $Re$ , though an inverse relationship is found between maximum speed up and aspect ratio as shown in Figure 37. No correlation is found between  $C_p$  and  $Re$ , though an inverse relationship is found between  $C_p$  and aspect ratio as shown in Figure 38.

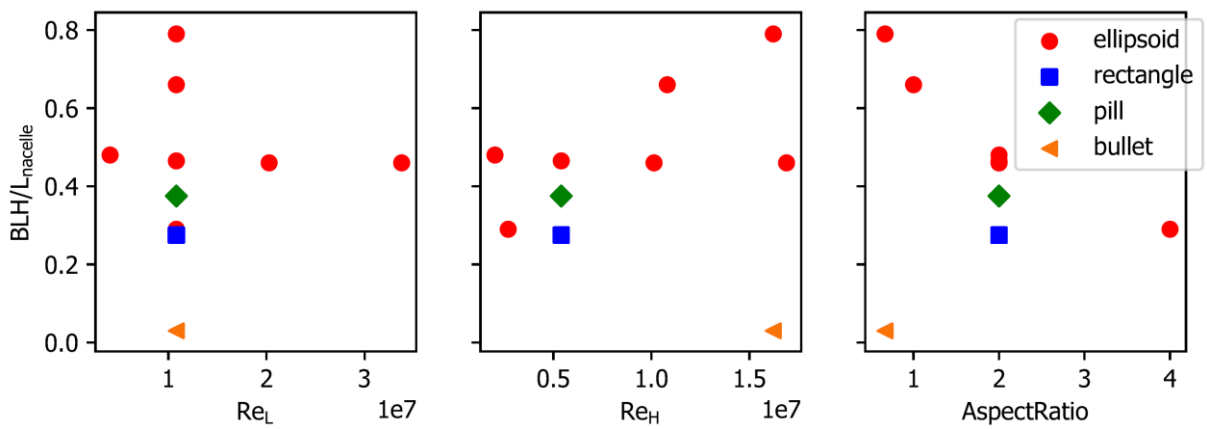


Figure 36  $BLH$  from CFD vs.  $Re_L$ ,  $Re_H$ , and aspect ratio for all nacelles.

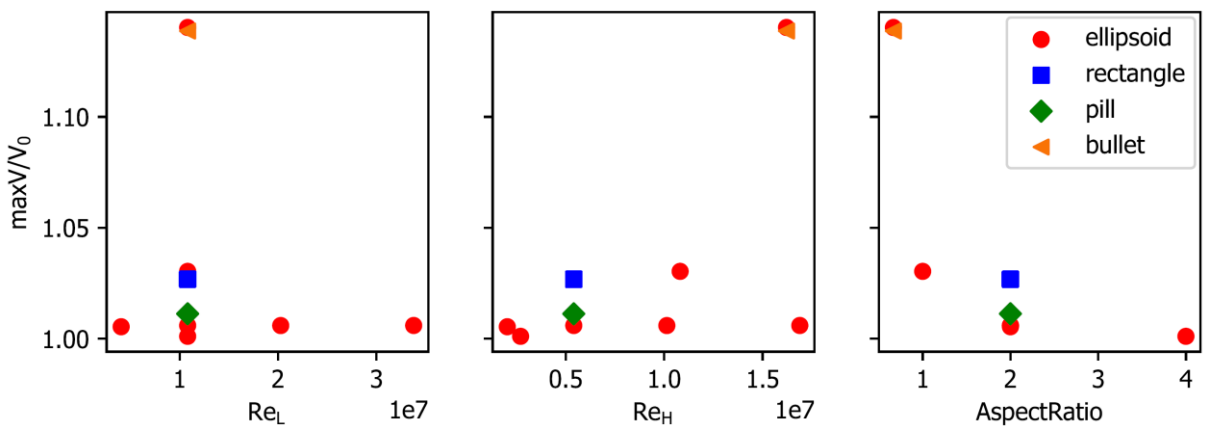


Figure 37 Maximum speed-up from CFD vs.  $Re_L$ ,  $Re_H$ , and aspect ratio for all nacelles

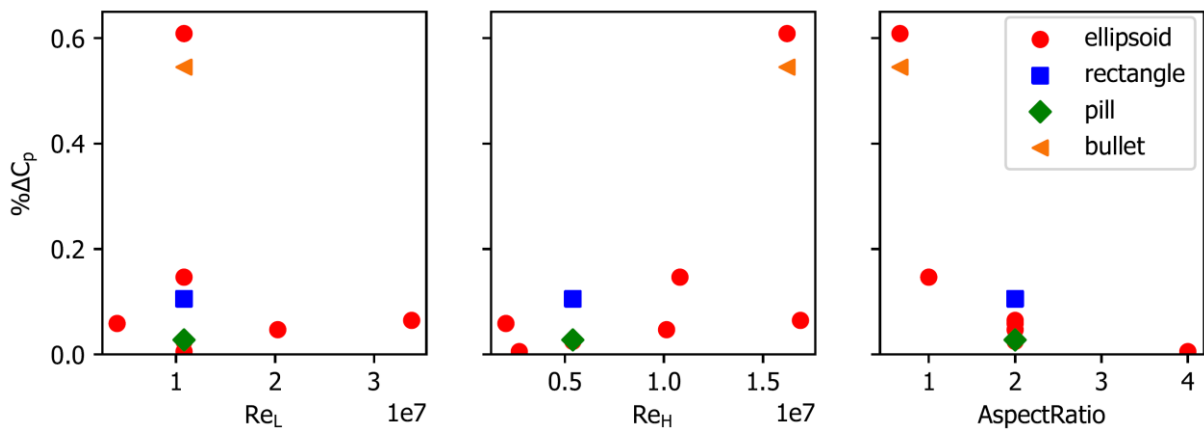


Figure 38 Rotor  $C_p$  in CFD flow field vs.  $Re_L$ ,  $Re_H$ , and aspect ratio for all nacelles

#### 4.5 Conclusion

Nacelle blockage effects on rotor loads and performance were found to be insignificant ( $<0.5\%$ ) for all except low-aspect-ratio nacelles. In all cases studied, nacelle blockage was seen to increase rotor loads and performance. The potential-flow engineering model developed here has negligible (sub-millisecond) computational cost.

The engineering model was validated against CFD, yielding like BEM results, with both models yielding  $C_p$  within 0.7% for all runs. For cases with the most significant blockage effects (20 x 30-m ellipsoid and bullet), the relative error in  $C_p$  between the two models was within 1% and 11%, respectively.

The EM struggled to match the blockage effects of some non-ellipsoid nacelles (rectangular prism and pill). A wake model was considered for integration into the EM but rejected because the EM consistently yielded lower changes in rotor performance than CFD, and the wake model would increase this disparity. Finally, the original EM method was not applicable for nacelles with an aspect ratio of  $>1$ , and the oversize ellipsoid method modification was used. The EM should be expanded to handle different and more complex geometries. This EM may be implemented in the OpenFAST [18] code to facilitate downwind turbine design in the future.

## 5. PASSIVE YAW IDLING MODEL AND CONDITIONS

### 5.1 Introduction

An idling condition in extreme wind speed is one of the most severe conditions in the design of wind turbines. Passive yaw (or free yaw) control is one of the promising methods to reduce extreme loads of downwind turbines in the storm condition. In the international standards and guidelines as IEC 61400-1 [22], for active yaw control, it is specified to consider yaw misalignment of up to  $\pm 15$  degrees in steady wind model and  $\pm 8$  degrees in turbulent wind model in storm standby condition. On the other hand, for passive yaw control, turbulent wind model should be used as the yaw misalignment is governed by the turbulent wind direction and the turbine yaw response. However, there is no description about the concrete analysis method. A load calculation method of wind turbine response and loads in passive yaw idling in storms is proposed and verified by the measurement data.

### 5.2 Recommendation

Here, the following analysis method is proposed.

- 1) As for wind direction, in addition to the short cycle fluctuation calculated from the turbulence model, change rate of average wind direction assumed in storm standby condition is set as constant.
- 2) Yaw misalignment is acquired from dynamic analysis according to the settings of wind speed, wind direction, wind turbine yaw response and so on.

The outline of the recommendation is summarized in Figure 39 by the comparison with the previous procedure.

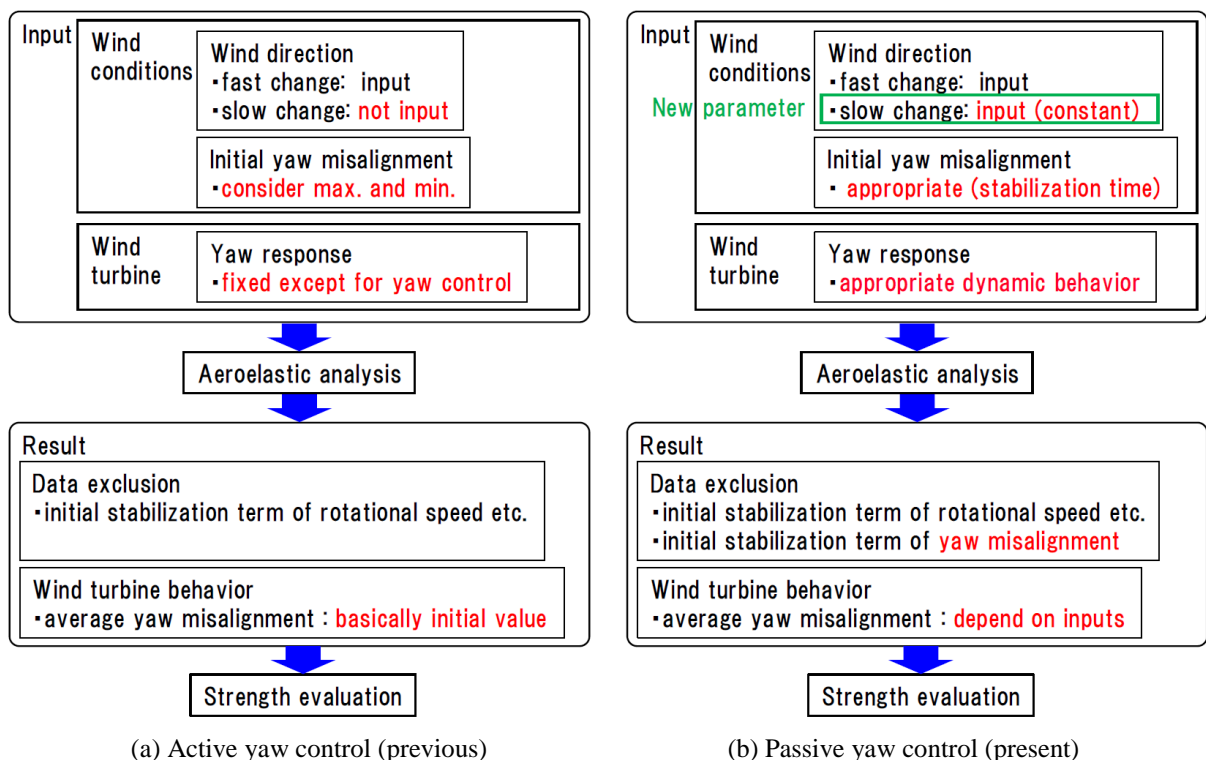


Figure 39 Recommendation for load calculation of passive yaw idling in storm.

### 5.3 Validation by the Measurement

The procedure recommended in the previous section is validated by the actual measurement data acquired in 2 units of 2-MW downwind turbine (model HTW2.0-80).

#### 5.3.1 Measurement data

Figure 40 shows the time history of wind speed and wind direction measured on nacelle and nacelle angle during typhoon passing. Figure 41 shows its 10 min averaged values. The wind speed gradually increased, and it turned

to decrease after observing the instantaneous maximum wind speed of 61.2 m/s around 14.4 o'clock. The wind direction is approximately constant at about 130 degrees until 13.2 o'clock, then turned to increase, and it is approximately constant at about 240 degrees after 15.1 o'clock. The nacelle direction follows the wind direction slightly behind by the passive yaw control. The target time in the subsequent analysis is 13.5 to 14.5 o'clock when the wind speed is high, and the change rate of wind direction is substantially constant.

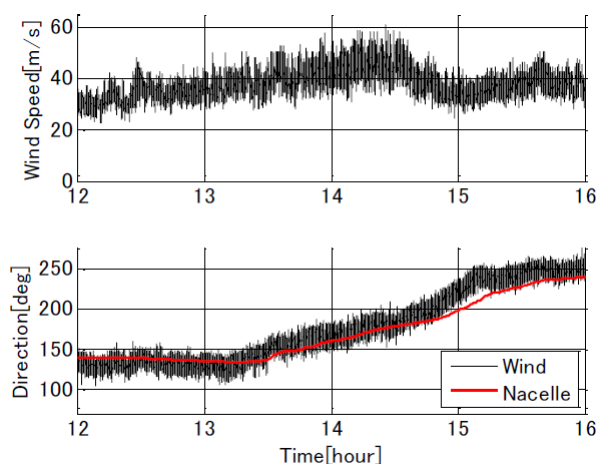


Figure 40 Wind speed, wind direction and nacelle yaw direction in a typhoon.

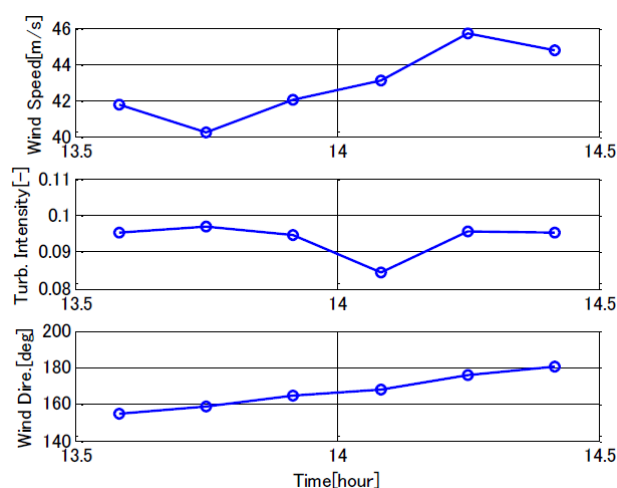


Figure 41 10 min average wind speed, turbulence intensity, and wind direction in a typhoon.

### 5.3.2 Analysis condition

Table 4 shows the analysis conditions which are basically based on actual measurement data shown Figure 40. The conditions which could not be extrapolated from actual measurement data are assumed considering the topographic characteristics of the site. For wind speed and wind direction, Kaimal spectrum is assumed, and only statistical values are fitted instead of time histories because it is considered that only statistical values of wind condition can be available at the design phase. The evaluation was performed statistically on the analysis results of six random number seeds. The average wind speeds were 40 and 44 m/s and the turbulence intensity was taken as the average value in the target period. As for the standard deviation of wind direction, the fluctuation components of actual measurement cannot be trusted because the vane type sensor was used. Therefore, the ratio of the three standard deviations of the wind speed was set to 1:0.8:0.5 which is the standard value in the topography of the target site (flat terrain). The change rate of wind direction is set as the mean value of the target period as constant. The initial yaw misalignment is set as the reverse sign of the change rate of wind direction in order to reduce the stabilization time of the yaw misalignment. The wind shear exponent was set to 0.11 which is common at the extreme wind speed condition.

The flow inclination was set to 0 degree due to sea wind. The yaw brake torque was set for dynamic and static friction, but it was confirmed that the influence of static friction was not so large. The analysis time was 910 seconds, and data for 310 to 910 seconds after yaw misalignment stabilized was used for evaluation.

Table 4 Analysis conditions for verification.

Wind turbine model	HTW2.0-80
Turbulence model	Kaimal spectral
Turbulence seed number	6
Average wind speed	40, 44m/s
Turbulence intensity	9.4%
Turbulence 3D component	$\sigma_1: \sigma_2: \sigma_3=1:0.8:0.5$
Change rate of wind direction	0.0087deg./s(constant)
Initial yaw misalignment	-10deg.
Wind shear ( $\alpha$ )	0.11
Inclination	0deg.
Yaw brake torque	Static+dynamic friction
Analysis time	910s(Evaluation period: 310~910s)

### 5.3.3 Yaw misalignment evaluation

An example of the analyzed time history is shown in Figure 42. The wind direction fluctuates in a short cycle and change in the positive direction on the average. The nacelle angle follows it slightly behind. After 100 seconds, the yaw misalignment is almost constant. Figure 43 shows the comparison between the actual measurement and the analysis result of yaw misalignment with respect to the 10 min average wind speeds. At a low wind speed of less than 40 m/s, the yaw misalignment is relatively large due to weak wind direction followability by passive yaw control, but it converges to a smaller value as the wind speed increases.

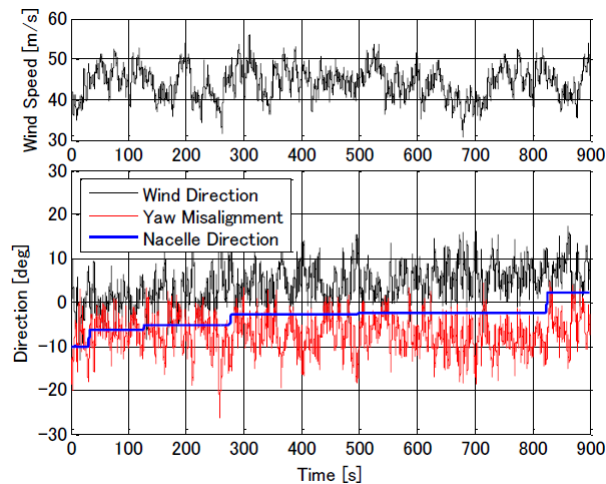


Figure 42 Time history of wind speed, wind directions, yaw misalignment, and nacelle direction.

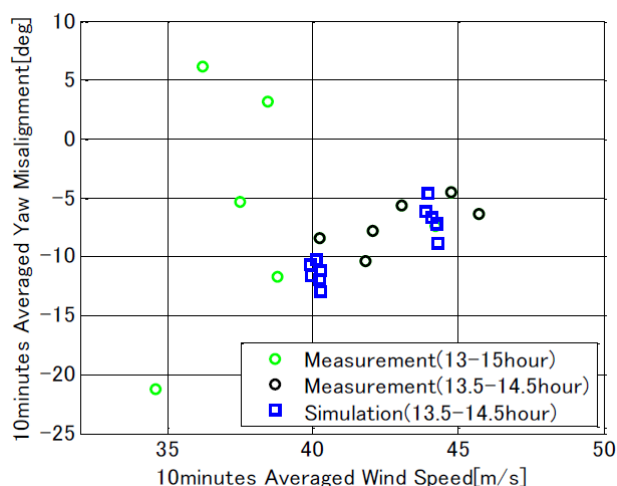


Figure 43 10 min average wind speed to yaw misalignment.

#### 5.4.4 Load evaluation

The comparison was made between analysis and actual measurement for the blade flapwise bending moment, which is the main load of the wind turbine and is often critical in storm standby condition. In actual measurements, optical fiber type strain gauges were installed on the pressure and suction side of the blade root part, and the flap bending was calculated from the measurement data. The values were normalized by the maximum value in the wind turbine design.

Figure 44 shows the comparison analysis and actual measurement for 10 min statistical values of flap bending. Three points each correspond to three blades. The predicted average and minimum values are in good agreement with the measured values. The predicted maximum values are a slightly higher than the measured values, so analysis is somewhat on the safe side.

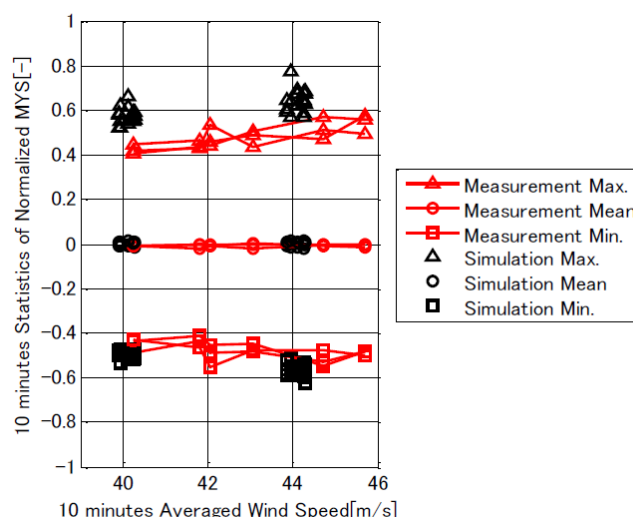


Figure 44 Comparison of predicted and measured blade flapwise bending moment.

## 5.5 Conclusions

Regarding the load evaluation in passive yaw control, the following results were obtained.

- 1) The method for evaluating wind load in passive yaw idling in storms, which takes the change rate of wind direction into account, was proposed.
- 2) The blade flapwise bending moment predicted by aeroelastic analysis with the proposed method was in good agreement with the actual measurement about average and minimum values and was slightly larger about maximum values.

- 3) The influence of the change rate of wind direction was investigated by aeroelastic analysis. It was shown that the imbalance of aerodynamic force between left and right side of rotor affects the wind turbine behavior and ultimate loads.
- 4) The possibility that the blade extreme loads could be reduced in idling in storm condition by the passive yaw control was shown.

## 6. SCALING BENEFITS OF DOWNWIND TURBINES

### 6.1 Introduction

Downwind turbine is the promising concept for future super-large wind turbines as it allows more flexible blades than upwind turbines. One of the effective countermeasures of upwind turbines is pre-bending of the blade to keep the enough clearance between the blade and the tower. To discuss about the pros and cons of the rotor positions, the effects of pre-bending and the tower shadow effect should be considered. The system engineering model in Section 2.5 was used for the downwind turbine model. Levelized cost of electricity (LCOE) was discussed about the downwind turbines by the comparison with three different conditions for pre-bending for 10 MW wind turbines.

This section is based on Namura and Shinozaki [23].

### 6.2 Methodology

#### 6.2.1 Fatigue Damage Evaluation

WISDEM [16] evaluates fatigue damage constraint as follows.

$$n/N < D_{limit} \quad (37)$$

where  $D_{limit}$  is an allowable fatigue damage,  $N$  is the number of cycles to failure when the load whose amplitude equals damage equivalent load (DEL) acts on the blade, and  $n$  is the number of cycles to calculate DEL. Note that only  $N$  is a variable calculated from DEL and the blade design while  $D_{limit} \leq 1$  is a design parameter and the arbitrary constant  $n = 6.3 \times 10^8 (= 20 \times 365.25 \times 24 \times 60 \times 60)$  here.  $N$  for blade structural components, including spar cap and trailing edge (TE) panel is calculated as

$$N = \left( \frac{\epsilon_{ult}}{\gamma_{del} \epsilon_{del}} \right)^m \quad (38)$$

where

$$\epsilon_{del} = \frac{M_{del} y_{str}}{EI_{str}}$$

$\epsilon_{ult}$  is the ultimate strain of the blade material,  $\gamma_{del}$  is the total safety factor,  $m$  is the S-N curve negative slope,  $M_{del}$  is the DEL of the bending moment in the evaluation direction (flapwise for spar cap and edgewise for TE panel),  $y_{str}$  is the moment arm between the blade pitch axis and the evaluation point on the spar cap or TE panel, and  $EI_{str}$  is bending stiffness of the blade in the evaluation direction.  $\epsilon_{ult}$ ,  $m$ , and  $\gamma_{del}$  can be determined from material properties and standards.  $y_{str}$  and  $EI_{str}$  can be calculated from structural design of the blade. Original WISDEM gives  $M_{del}$  of a reference turbine, though load difference between the optimized and reference blades is ignored in this way.

$M_{del}$  is estimated from steady state loads at four rotor azimuth angles here. Let  $M_a(r, V)$  be the bending moment in the evaluation direction when the blade azimuth angle, blade radial section, and hub wind speed are  $a$ ,  $r$ , and  $V$ , respectively, moment amplitude  $\Delta M(r, V)$  is calculated as

$$\Delta M(r, V) = \frac{1}{2} \left[ \max_a (M_a(r, V)) - \min_a (M_a(r, V)) \right] \quad (a = 0, 90, 180, 270 \text{ degrees}) \quad (39)$$

$M_a(r, V)$  is evaluated from the BEM analyses considering blade pitch angles described later, and  $M_{180}(r, V)$  includes the tower shadow and potential flow effects.  $M_{del}$  at  $r$ ,  $M_{del}(r)$ , is estimated from  $\Delta M(r, V)$ , normalized wind speeds histogram  $f(V)$ , and rotational speed of the rotor  $\omega(V) \text{ min}^{-1}$  as

$$M_{del}(r) = \left[ \frac{1}{n} \int_{V_{in}}^{V_{out}} \Delta M(r, V)^m f(V) \omega(V) n_{time} dV \right]^{\frac{1}{m}} \quad (40)$$

where  $V_{in}$  and  $V_{out}$  are cut-in and cut-out wind speeds and  $n_{time} = 20 \times 365.25 \times 24 \times 60$  minutes. Turbulence and vibration effects on DEL should be included in  $\gamma_{del}$  because Equation (40) ignores them.

The blade pitch angles above rated wind speed were estimated by comparing rotational forces at a blade cross-section in the above rated condition. The tangential force  $F$ , induced by local lift force of an airfoil at  $r$  is as follows if drag force and induced velocities are disregarded.

$$F = C_l \frac{1}{2} \rho c [V^2 + (r\omega_{rated})^2] \sin\phi \quad (41)$$

where,

$$C_l = C_{l0} + \frac{\partial C_l}{\partial \alpha} (\phi - \theta)$$

$\rho$ ,  $c$ ,  $\omega_{rated}$ ,  $\phi$ ,  $\theta$ ,  $C_l$ ,  $C_{l0}$ , and  $\partial C_l / \partial \alpha$  are air density, chord length, rotor speed, inflow angle, pitch angle, lift coefficient, lift coefficient at the zero angle of attack, and lift slope, respectively.  $F$  in above rated condition is assumed to be constant as the rated wind speed condition. The subscript “rated” is the values at the rated wind speed, this assumption gives the following equation to estimate  $\theta$  in the above rated conditions.

$$\theta = \phi + C \left[ 1 - \frac{\{(V_{rated} - V_0)^2 + (R\omega_{rated})^2\} (1 + C^{-1} \phi_{rated}) \sin \phi_{rated}}{\{V^2 + (R\omega_{rated})^2\} \sin \phi} \right] \quad (42)$$

where

$$C = C_{l0} \left[ \frac{\partial C_l}{\partial \alpha} \right]^{-1}$$

$$\phi = \tan^{-1} \left( \frac{V}{R\omega_{rated}} \right)$$

$$\phi_{rated} = \tan^{-1} \left( \frac{V_{rated} - V_0}{R\omega_{rated}} \right)$$

$$V_0 = 1 \text{ [m/s]}$$

$r$  is replaced by rotor radius  $R$ .  $V_0$  is a gap between the rated wind speed ( $V_{rated}$ ) and the wind speed at which the pitch control begins ( $V_{rated} - V_0$ ). Equation (42) can include the effects of induced velocities by multiplying  $\phi$  and  $\phi_{rated}$  by  $2/3$  though we ignored them due to better estimation accuracy in 10 MW turbines without it. The parameter  $C$  was determined by fitting Equation (42) to pitch schedules of the NREL 5 MW reference turbine and some other turbines. Equation (42) enabled to estimate  $M_a(r, V)$  with reasonable accuracy in the above rated condition.

### 6.2.2 Ultimate Load Approximation

The ultimate load for the blade strength is assumed to occur when the lift force of the non-rotating feathered blade becomes maximum with the EWM and instantaneous yaw misalignment due to turbulence. This condition can happen in both DLC 6.1 and DLC 6.2. We approximated the ultimate load in the DLC 6.1 because the DLC 6.1 includes normal safety factor of 1.35 and results in severer load than the DLC 6.2. In the prior analyses, a non-rotating blade of the NREL 5MW reference turbine showed its maximum lift force at a blade tip angle of attack of

19 degrees. Thus, blade loads are calculated at the blade tip angle of attack of 19 degrees, hub wind speed of  $1.4V_{ref}$  ( $V_{ref} = 50$  m/s for IEC class I turbines in this study), and rotor azimuth angle of 0 degrees with steady state BEM analyses as the ultimate loads with the 50-year EWM. Kiyoki et al. measured yaw misalignment of a 2 MW downwind turbine at an extreme wind condition caused by typhoons and revealed that the instantaneous yaw misalignment around 19 degrees frequently appeared [24]. The blade tip angle of attack should reach 19 degrees in this condition.

### 6.3 Optimization Conditions

Design optimization was conducted for onshore 10 MW downwind and upwind turbines under the IEC Class IA condition. To investigate the effect of prebend on LCOE of the upwind turbines, two design cases were prepared. Case-1 assumed realistic prebend up to 6 m according to [25,26] while Case-2 allowed the upwind turbines to have optimal prebend up to 20 m balancing power production and cost reduction. The downwind turbines did not have prebend to keep large clearance between the blades and tower and prevent the blades from striking to the tower at shutdowns. In both downwind and upwind turbines, tilt and cone angles of the rotor were fixed at 6 degrees and 4 degrees, respectively, as well as Bortolotti et al. [26]. The optimal blade deflection was determined in two steps to reduce the computation for the convergence. In the first stage, optimization in the Case-1 was conducted without the deflection, and tentative deflection at 70% of the rated wind speed, which gave a reasonable approximation of annual energy production (AEP) [17], was obtained. Then, the tentative deflection was introduced to the second stage of optimization in the Case-1 and -2. The Case-1 introduced 90% of the tentative deflection of the downwind turbines and 100% of the tentative deflection of upwind turbines to the corresponding turbines while the Case-2 introduced 90% of the tentative deflection of downwind turbines to the upwind turbines. 90% of the tentative deflection gave reasonable approximation in flexible blades.

The objective function, constraints, and design variables of the design optimization were summarized in Table 5. Design of blade and tower was optimized to minimize LCOE while drivetrain with a three-stage gearbox was implicitly optimized to minimize its mass through DriveSE in WISDEM. The optimization was conducted with various blade lengths from 75-105 m. LCOE minimization was the only one objective function in this study. The onshore cost model in WISDEM was used to evaluate LCOE due to its reliability even though 10 MW wind turbines are usually employed at offshore sites. Onshore cost model did not affect optimization results because most parts of the cost models except turbine cost were functions of rated power fixed at 10 MW. Hence, LCOE was minimized by minimizing the turbine cost and maximizing AEP.

Table 5 Objective function, constraints, and design variables of design optimization.

Objective function		LCOE (minimization)
Constraints	Blade	Ultimate, buckling, and fatigue strength, natural frequency, angle of attack, tip speed, root diameter, and deflection (upwind)
	Tower	Ultimate and buckling strength, natural frequency, manufacturability, and weldability
Design variables	Blade	Chord, twist, airfoil, spar cap thickness, TE panel thickness, and prebend (upwind)
	Tower	Outer diameter, wall thickness, and waist position
	Others	Tip speed ratio, rated rotational speed

Most of the constraints were same as those used by Ning and Petch [17], as well as the material properties provided by WISDEM and the Sandia National Laboratories [27]. The partial safety factor for DEL was set to 2.0 to include turbulence and vibration effects. Five constraints were added and modified: fatigue strength, angle of attack, tip speed, blade root diameter, and deflection. The DEL estimation was added for the blades while the fatigue damage of the tower, which was an inactivated constraint, was eliminated. The maximum tip speed was limited below 100 m/s. The blade root diameter should be greater than 90% of hub diameter, which was 5% of the blade length. The maximum blade tip deflection should be smaller than 70% of clearance between the unloaded blades and tower for upwind turbines.

The design variables were mainly related to the blades and tower because the drivetrain was implicitly optimized in WISDEM. Spar cap and TE panel thicknesses were used as design variables while shell and spar web were simply scaled up from those of the NREL 5MW reference turbine. The number of design variables was 42 for downwind turbines and 45 for upwind turbines (including three for prebend). The hub height was not a design variable and computed as  $R + 20$  m. The overhang was approximated as a sum of the hub diameter and tower top radius.

## 6.4 Results and Discussion

### 6.4.1 Performance of optimized wind turbines

The optimized downwind turbines and upwind turbines in the Case-1 and -2 were compared to validate the superiority of the downwind turbines with the flexible blades in the IEC class IA condition. Figure 45 shows various aspects of performance of downwind and upwind turbines: LCOE, rotor AEP, blade mass, RNA mass, tower mass, blade tip deflection at 70% of the rated wind speed, maximum blade tip deflection, and the blade tip prebending. The downwind turbines with a rotor diameter over 164 m show the superiority in LCOE to the upwind turbines with conventional prebend (Case-1) and achieve their lowest LCOE at the rotor diameter of 194.75 m. This is derived from 15-17% lighter and more flexible blades installed in the downwind turbines. These lighter blades also decrease the RNA mass including hub and nacelle components by 5-7%. On the other hand, blade structure of the upwind turbines in the Case-1 is constrained by the clearance between the blades and tower although prebend up to 6 m is fully applied.

Another advantage of the downwind turbines with flexible blades is a smaller thrust force due to the rotor tilt and cone angles and deflection toward downstream whereas AEP is also reduced. This smaller thrust force enables the downwind turbines to have comparable tower mass to the upwind turbines. The other important feature is a smaller distance between the tower axis and the center of gravity of the RNA (1 m) than that in the 5 MW turbines (2 m). The smaller distance is derived from the nacelle as heavy as the tower. This will be the main difference with the results of Ning and Petch [4], where heavier towers of the 5 MW downwind turbines increased their LCOE.

In the downwind turbines, the deflection toward the tower at the shutdown should be considered. Figure 45 (g) includes the clearance between the unloaded blades and tower of the downwind turbines. The tower-strike can be avoided by designing a suitable shutdown process because the clearance is greater than 90% of the maximum blade tip deflection. Besides, the downwind turbines can adopt larger tilt and cone angles or prebend toward downstream to make additional clearance [28, 29]. In fact, commercial downwind turbines have tilt and cone angles of 8 degrees and 5 degrees, respectively [30]. These angles give additional 5 m clearance to the downwind turbine with the rotor diameter of 194.75 m.

The upwind turbines with optimal prebend (Case-2) have comparable LCOE to the downwind turbines and achieve the lowest LCOE at the rotor diameter of 184.5 m, although the upwind turbine with the lowest LCOE requires significantly large prebend of 11 m. These two took different ways to achieve their lowest LCOE. The downwind turbines, which can adopt the lighter rotor with lower thrust, utilize lighter RNA to achieve lower cost while the upwind turbines keep AEP higher. The downwind turbines may have advantages when turbines are installed in offshore farms or farms with earthquakes. The smaller thrust force will reduce the bending moment and cost of structures under the sea in offshore farms. In earthquake regions, the lighter RNA can reduce the tower mass and cost which are dominated by ultimate loads of earthquakes instead of the DLC 1.3 in this study.

Figure 45 (f) compares the 90% and 100% of tentative deflection used in load computation and blade tip deflection obtained in the second stage of the optimization. The deflection of downwind and upwind turbines is well approximated while underestimation sometimes occurs.

In this study, the only DLC 1.3 and DLC 6.1 were approximated by steady state aero-structural analyses, though all DLCs should be evaluated in the real wind turbine design. Thus, the feasibility of the optimized wind turbines at the other DLCs represented by the DLC 1.4 and DLC 5.1, where the tip deflection of upwind turbines and deflection toward the tower for downwind turbines can be maximized, respectively, should be validated with unsteady aero-structural analyses. Gusts with direction change at the DLC 1.4 may increase the angle of attack and maximum tip deflection of the upwind turbine blade. This is because DLC 1.3 approximated by  $V_{rated} + 3\sigma_{ETM}$  increases the angle of attack at the 80% blade position by 14 degrees in the present design condition, which is too large for the airfoils to have their highest  $C_l$ . On the other hand, the large clearance comparable to the

maximum tip deflection at  $V_{rated} + 3\sigma_{ETM}$  with the ETM may prevent the downwind turbines from tower-strike at the DLC 5.1 as it assumes emergency shutdowns with the normal turbulence model.

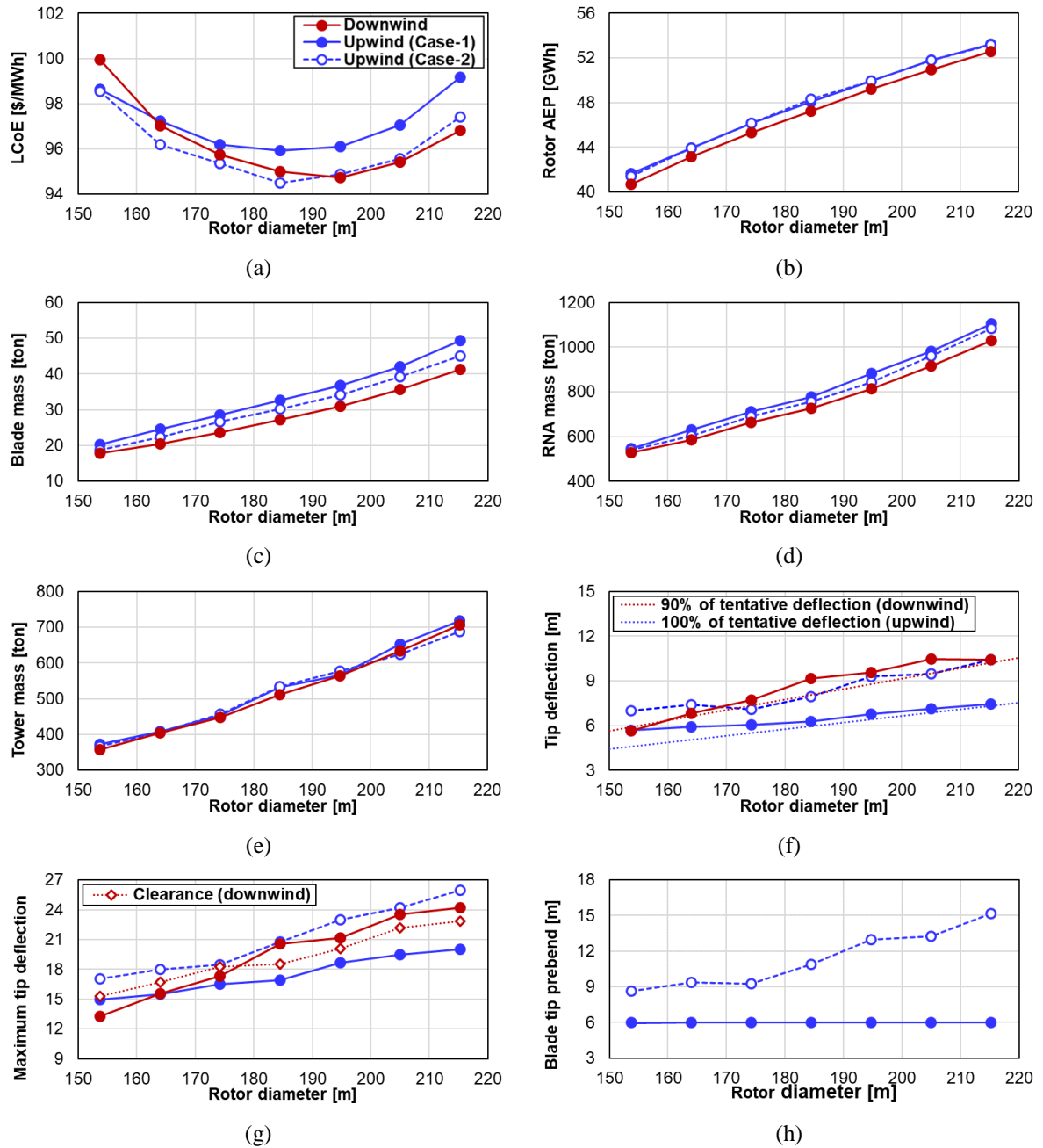


Figure 45 Performance of optimized wind turbines: LCOE (a), rotor AEP (b), blade mass (c), RNA mass (d), tower mass (e), blade tip deflection at 70% of the rated wind speed (f), maximum blade tip deflection (g), and blade tip prebend (h).

### 6.4.2 Optimized blade shapes and characteristics

To reveal features of the optimized downwind turbine, blade shapes and characteristics of the representative downwind and upwind turbines with a rotor diameter of 184.5 m where the upwind turbines achieve their lowest LCOE, were compared. Figure 46 shows chord length, twist angle, spar cap thickness, total deflection (tentative deflection minus prebend), edgewise DEL, and flapwise DEL of the representative turbines. The downwind turbine has clearly different features compared to upwind turbines. Chord length of the downwind turbine is smaller than upwind turbines. Smaller chord length derives lighter blades while it requires smaller twist angle to increase the angle of attack. The angles of attack of downwind and two upwind (both Case-1 and -2) turbines at their outboard

is approximately 5 degrees and 4 degrees, respectively. The upwind turbine in the Case-1 has a small angle of attack around 3 degrees at the blade tip to reduce flapwise bending moment and deflection. Besides, the downwind turbine can adopt thinner spar cap than the upwind turbines as shown in Figure 46 (c). The blade structure of the downwind turbine is mainly constrained by the ultimate compressive strength at the spar cap and fatigue damage at the TE panel. On the other hand, activated constraints in the two upwind turbines are the maximum blade tip deflection for the spar cap and buckling at the TE panel.

Estimated DEL in Figure 46 (e) and (f) reflects the design feature of each wind turbine. The edgewise DEL follows the mass of the blades though the downwind turbine with the smallest edgewise DEL is severely constrained by the fatigue damage at the TE panel. This is because the small chord length significantly decreases edgewise stiffness and increases strain amplitude. The flapwise DEL is correlated with the wind speed decay induced by the tower shadow and potential flow. The upwind turbine in the Case-1 has the largest flapwise DEL due to the small clearance between the loaded blades and tower, which is derived from prebend canceled by deflection as shown in Figure 46 (d). The upwind turbine in the Case-2 has smaller flapwise DEL than that in the Case-1 because the large prebend of 11 m is not canceled by deflection of 8 m and makes an additional 3 m clearance. Flapwise DEL of the downwind turbine is as small as that of the upwind turbine in the Case-2. Its flexible blades make large clearance to alleviate the wind speed decay induced by the tower shadow.

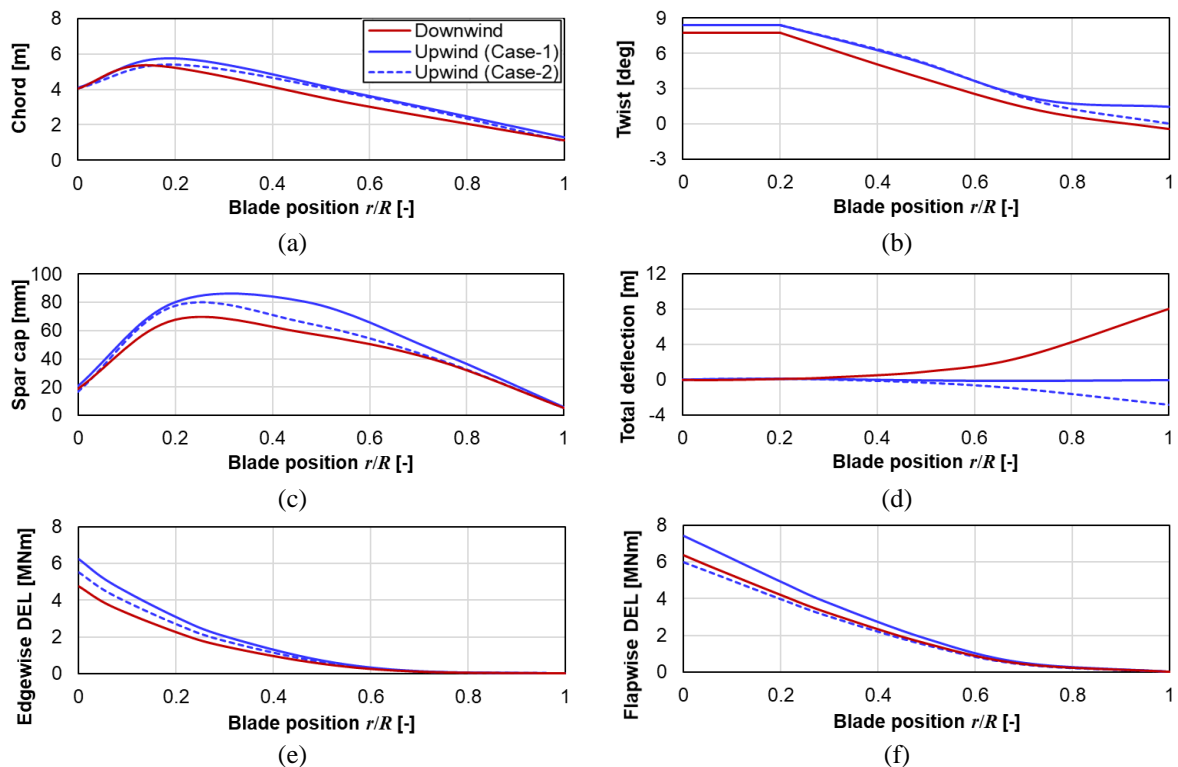


Figure 46 Blade shapes and characteristics of the representative wind turbines: chord (a), twist (b), spar cap thickness (c), total deflection (d), edgewise DEL (e), and flapwise DEL (f).

## 6.5 Conclusions

The designs of 10 MW downwind and upwind turbines at IEC class IA, with pre-bent blade assumed to minimize LCOE at IEC class IA condition were compared. The downwind turbines showed better LCOE than the upwind turbines due to its lighter and flexible blades. Since these blades also decreased the thrust force and RNA mass, the downwind turbines had an advantage in cost with AEP sacrificed. The smaller thrust force and RNA mass of downwind turbines are advantageous in offshore farms and farms with earthquakes, respectively. The upwind turbines required significantly large prebend of 11 m to obtain comparable LCOE to the downwind turbines. The cost influences on the production and transportation of the pre-bent blades are not considered here.

## 7. FURTHER OPPORTUNITIES OF DOWNWIND TURBINES

### 7.1 Introduction

Downwind rotor fell out of favor historically because of their higher acoustic emission and fatigue loads, both of which occurred in older designs when the blades passing through the tower wake. However, as modern commercial wind turbines continuously grow in size aggressively, the design of upwind turbine rotors is increasingly constrained by maximum allowable blade-tip deflections to avoid the tower strike, which is much less of a concern for downwind wind turbines. Because modern wind turbines are also characterized by much slenderer blade and tower structures than older kilowatt-scale machines, the prior concerns about noise and fatigue loads are less pressing and downwind technology has seen a revival of interest.

Downwind rotor is promising for future super-large wind turbines, due to the technical features which are unique in downwind turbines, such as 1) lighter-elastic blades, 2) larger rotor-tower clearance, 3) yawing stability, 4) negative rotor tilt, etc. This chapter highlights several untapped opportunities for downwind wind turbine technologies that cannot be easily evaluated with current Multi-Disciplinary Analysis and Optimization (MDAO) or aero-servo-elastic models briefly. Future research and development are recommended to fully assess the potential of these concepts.

This chapter is based on Anderson, et al. [31].

### 7.2 Methodology

#### 7.2.1 Design Method

The design studies were conducted in WISDEM used roughly the same approach as Ning and Petch [17], with new cost models shown in the next subsection. The analysis also differs in the additional aeroelastic analysis with OpenFAST and the ROSCO controller, which are run after the design optimizations are completed. Compared to the steady-state, rigid-blade simulation models embedded in WISDEM, OpenFAST predicts the loading and performance of a wind turbine design at a higher level of fidelity, modeling unsteady aerodynamics, aeroelastic dynamics, and the effects of a dynamic controlling. The controller, ROSCO, has its own toolbox to automatically tune gains, set points, and other key parameters based on physical properties of the rotor design [32,33,34]. This is a critical feature when conducting design exploration studies as the rotor geometry and mass properties can change significantly over the course of an optimization.

#### 7.2.2 Cost Model

In the LCOE equation, the turbine capital cost (TCC) was computed using a detailed blade cost model [35], and the remaining component costs were estimated by the NREL Cost and Scaling Model [36]. The fixed-charge rate (FCR), balance-of-station (BOS), and operation-and-maintenance expenditures (OPEX) were 5.6%, \$3143/kW, and \$129/kWh, respectively, assuming fixed-bottom offshore plants [37], and were assumed to be the same for both the upwind and downwind configurations. Finally, AEP was calculated with an OpenFAST execution of DLC 1.1 which corresponds to standard operating conditions across the power curve, with six turbulent seeds per wind speed.

### 7.2.3 Reference Design

Hitachi 10 MW downwind turbine concept was adopted as the reference turbine. The general specifications are shown in Table 6.

Table 6 General specifications of the Hitachi 10 MW reference downwind turbine concept.

Parameter	Value	Unit
Power rating	10	MW
Turbine class	IEC Class 1A	—
Rotor orientation	Downwind	—
Number of blades	3	—
Control	Variable speed	—
Drivetrain	Gearbox	—
Gearbox ratio	40	—
Cut-in wind speed	4	m/s
Cut-out wind speed	25	m/s
Rated rotor speed	8.5	rpm
Rated wind speed	11	m/s
Maximum tip speed	90	m/s
Design tip-speed ratio	10	—
Rotor diameter	204	m
Hub diameter	4	m
Hub height	131.5	m
Blade tip prebend (toward the tower)	3	m

### 7.2.4 Rotor Redesign

#### (1) Design variables

Table 7 Design variables in the rotor design optimization.

Design quantity	# of active design variables	Fixed points
Twist	5	Root
Chord	4	Root and tip
Thickness spar cap suction	4	Root and tip
Thickness spar cap pressure	4	Root and tip
Tip-speed ratio	1	
<b>Total</b>	<b>19</b>	

#### (2) Design constraints

- Maximum allowable 2500 microstrains in the spar caps on suction and pressure sides along the span.
- Minimum 3-degree margin to stall, which was imposed below rated wind speed for the prescribed tip-speed ratio.
- Maximum chord of 6.6 m.
- First flap and edge blade modes greater than or less than the 3P (three per revolution) rotor harmonics.
- Minimum blade-tower clearance.

## 7.3 Optimization Results

### 7.3.1 Optimized Blades

The upwind turbine blade was optimized with the same cone and tilt angles of the downwind turbine, but without the tip deflection constraint. Figure 3 shows the comparison of blades optimized for upwind and downwind turbines. The final downwind turbine blade mass and cost were 42,500 kg and 567.3 k\$, which are 4.4% lighter and 6.3% cheaper than those of upwind turbine blade respectively, due to the shorter chord length and thinner spar caps. And the design of downwind turbine blade is driven by the spar cap strains in the present condition.

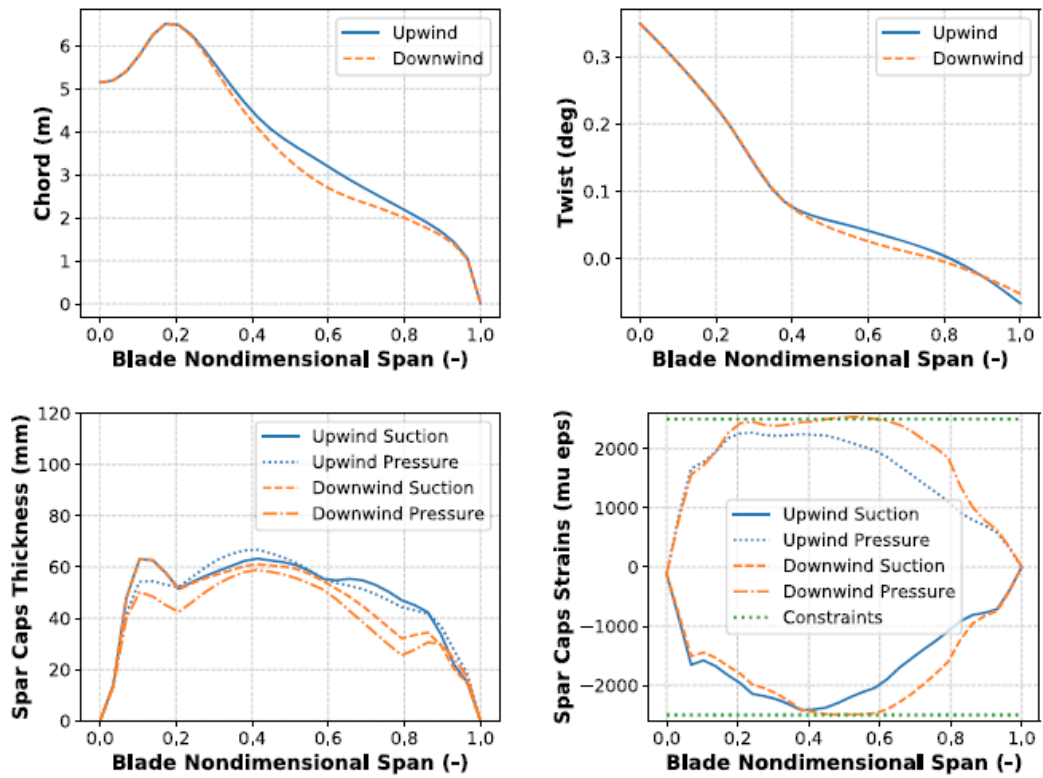


Figure 47 Comparison of upwind and downwind blades: (top left) chord length, (top right) twist angle, (bottom left) spar cap thickness, (bottom right) ultimate strains in the spar caps.

### 7.3.2 AEP Comparison

Power curves calculated by the aero-servo-elastic OpenFAST simulations are shown in Figure 48. The downwind turbine shows slightly lower power than the upwind turbine, by the reduced swept area during operational loading as shown in Figure 49. The result is consistent with prior findings [38,39]. It results in 1.2% lower AEP.

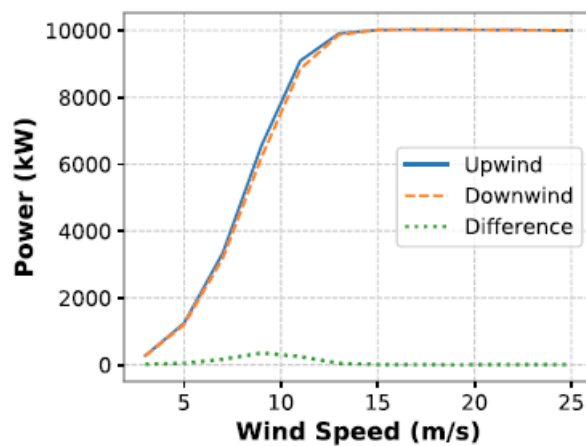


Figure 48 Comparison of power curves of upwind and downwind turbines.

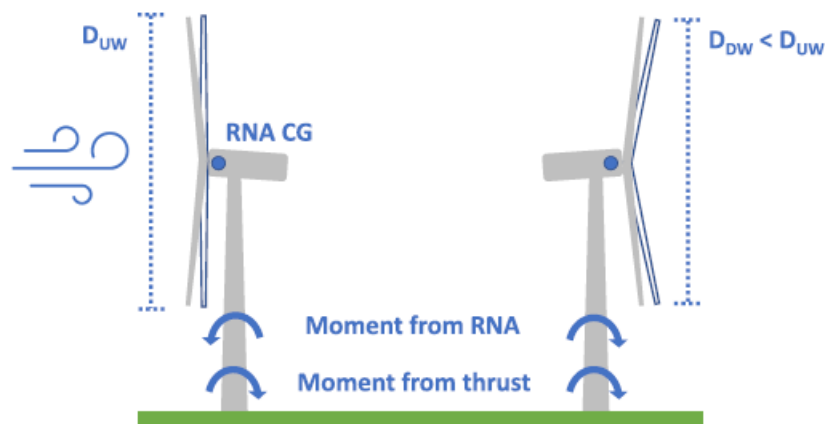


Figure 49 Swept area changes and base moment contributions of upwind (left) and downwind (right) turbines.

### 7.3.3 Load Comparison

A load comparison was performed to investigate how ultimate and fatigue loads from OpenFAST varied between the upwind and downwind designs. Ultimate and fatigue loads from six-turbulent seeds of DLCs 1.1 and 1.3, four wind speeds of DLC 1.4, and twelve wind speeds of DLC 1.54 are compared in Figure 50.

The rotor ultimate aerodynamic thrust (“Th” in the figure) and the blade root flapwise moments (BRF) decreased consistently in the downwind configuration. This is due to the lower rotor swept area, reducing the thrust and the centrifugal forces counteracting the aerodynamic thrust to reduce the flap moment of the coned rotor blades. Fatigue damage equivalent loads (DELs) of the rotor thrust (Th) and blade root flapwise bending moment (BRF) increased 5% and 2% because of the blade-tower wake interaction. On the other hands, DEL of the blade root edgewise bending moment (BRE) decreased as a result of the small blade mass, whereas the ultimate value increased. Finally, both the ultimate and fatigue shaft overturning moments decreased in the downwind 9% and 8% respectively as a result of a reduced rotor mass.

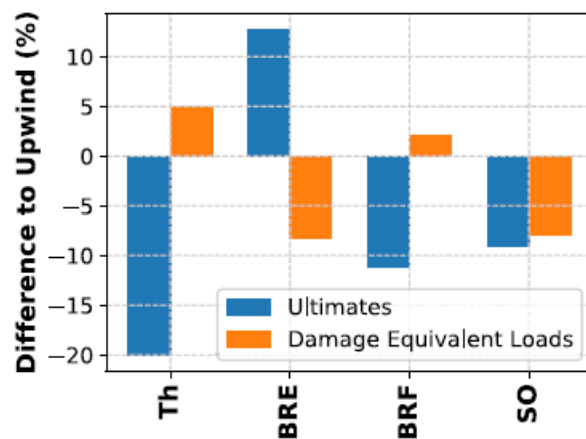


Figure 50 Comparison of ultimate and fatigue rotor loads between optimized downwind and upwind designs. Legend: (Th) rotor thrust, (BRE) blade root edgewise moment, (BRF) blade root flapwise moment, (SO) shaft overturning moment.

### 7.3.4 LCOE Comparison

The LCOE analysis results are summarized in Table 8. Nevertheless, the optimized solution was found to be fairly similar to the upwind, except for a slight increase in the tip-speed ratio of 10.4 and a corresponding slenderer chord distribution. With a reduction in blade mass, the costs of the nacelle system were also reduced by 1.3%, and the complete turbine capital cost reduction was 1.7%.

As a result, the LCOE of the downwind turbine 83.49\$/MWh is 0.9% more than the upwind turbine.

Table 8 LCOE analysis of the optimized designs.

Data	Upwind	Downwind
Number of turbines [-]	60	60
Machine rating [MW]	10	10
TCC [\$/kW]	1301	1283
BOS [\$/kW]*	3143	3143
OPEX [\$/kW]*	129	129
Park AEP [TWh]	2.74	2.71
FCR [%]*	5.6	5.6
LCOE [\$/MWh]	82.76	83.49

## 7.4 Sensitivity Studies

Sensitivity studies were conducted for some typical features of downwind turbines.

### 7.4.1 Passive Yawing

The yawing aerodynamic stability of downwind rotors can downsize the yaw actuators. Several works in literature have investigated the topic of free-yaw downwind rotors, both numerically [40,41] and experimentally with scaled wind tunnel models [42,43]. The experimental studies generally returned promising results, whereas the numerical studies found conditions where the free-yaw rotor generated large yaw misalignments and power losses. To help resolve this uncertainty, a sensitivity check was performed on the potential cost benefits of a free-yaw system, assuming 50% of the capital costs of the yaw system of the downwind turbine. Here, maintenance costs were not changed.

The analysis returned a minor impact on the LCOE about -0.17%. Unless significant benefits in terms of maintenance costs and/or reduced power losses from yaw misalignment can be identified and quantified in large multi-MW rotors, the advantages of passive yaw might be not large enough to justify the inherent risks of having no yaw actuator.

### 7.4.2 CG of RNA Effects on Tower and Foundation

As shown in Figure 49, the center of gravity (CG) or the rotor-nacelle assembly (RNA) of the baseline model is located at the rotor side from the tower center. And the gravity load of RNA makes the tower base fore-aft bending moment increased.

A sensitivity analysis was conducted for the position of the CG of the RNA of the downwind turbine as shown in Figure 51. It shows that if the CG of the RNA is less than +1.5m from the tower axis (positive toward the downwind rotor apex), the optimized downwind machine generates a lighter support structure. If the CG could be moved further upwind, on the opposite side of the tower centerline, the advantage increases significantly.

Wind turbine nacelles have historically been designed to place the CG of the RNA between the tower and rotor and have zero net moment on the nacelle at rated wind speed. Changing the first of the two paradigms by pushing the CG closer to the tower centerline, or event behind it, could have a significant impact on the downwind wind turbine capital cost.

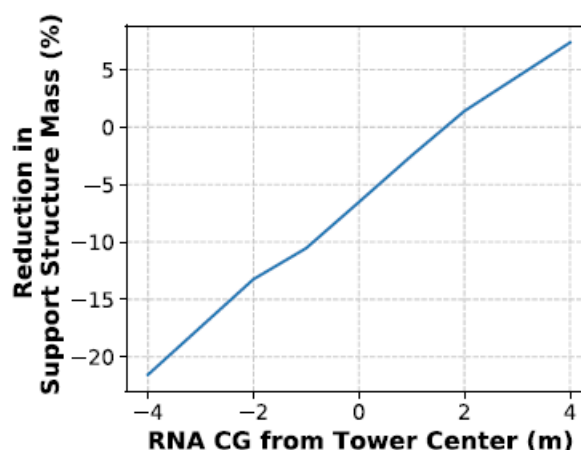


Figure 51 Reduction in support structure mass for a downwind wind turbine with varying positions of the CG of the RNA. CG position of 0 m corresponds to the tower centerline with positive toward the downwind rotor apex.

#### 7.4.3 Rotor Cone and Tilt Angles

A sensitivity study on the power and load effects from changing cone and tilt angles was conducted for the optimized downwind design. Higher values of the cone and tilt angles lead to lower values of AEP because of the smaller swept area, but there was no corresponding reduction in blade mass or cost as the blade design was still constrained by ultimate strains. On the other hand, with smaller cone and tilt angles also comes higher load amplitudes, which increase the risk of fatigue and aeroacoustics, even with modern designs and control strategies.

Notably, numerical and experimental studies have also considered highly coned downwind wind turbines, chasing the “load alignment” concept, where the loaded-blade axis aligns with the resultant thrust-centrifugal force vector to eliminate bending moments. The preliminary researches show similar trends as reduced capital costs from lighter blades and lower AEP [28,29].

### 7.5 Conclusions

Performances, loads, LCOEs of 10 MW upwind and downwind turbines compared through multidisciplinary design, analysis, and optimization (MDAO) studies. For the same rotor diameter, the downwind solution returns 4.4% lower blade mass, but the upwind rotor generates 1.2% higher AEP and 0.9% lower LCOE. This is mainly due to the reduced capture area when the downwind blades are loaded and is robust to key blade deflection constraint values or other variations in cone and positive rotor tilt. In terms of loads, downwind turbines decrease key ultimate loads, but see a mild increase in fatigue loading due to the blade passing in the tower wake. The impact of the location of the center of gravity of the rotor-nacelle-assembly (RNA) on the tower and foundation is investigated, showing that the redesign of nacelle could offer significant mass and cost savings in the substructure of downwind turbines.

Furthermore, sensitivity studies and literature survey show the following opportunities of downwind turbines.

- 1) Aerodynamics of Coned and Highly Flexible Rotors: Most of the previous research which compares upwind and downwind turbines are based on blade element momentum theory. A key assumption with the model is that the blades turn in the rotor plane with small blade deflections, which could easily be violated in a downwind configuration. As illustrated above, downwind rotors still offer promising parametric knobs that give more design freedom than the more tightly constrained upwind rotors. Higher fidelity aerodynamic solvers should be developed for more accurate comparison between downwind and upwind turbines on loads and performance. Vortex method, such as the free vortex wake model implemented in OpenFAST [44], is a promising candidate for that.
- 2) Advanced Controls: Controllers specifically tuned for downwind turbines could maximize the mass reduction of downwind turbines. The controller, which limits cut out wind speeds or de-rates at high wind speeds can reduce the blade deflections back toward the tower. And optimized shutdown maneuvers could also minimize

the clearance between the rotor and tower. Smart rotor with distributed aerodynamic control devices and individual pitch control could also reduce fatigue loads of downwind wind turbines.

- 3) Floating Offshore Wind Turbines: The thrust loads on floating offshore wind turbines make the substructures inclined. Downwind turbines, which has a negative tilt angle generally, are advantageous for floating offshore wind turbines, as the rotor-wind misalignment would be smaller in power production. The yawing stability is also advantageous for some specific floating offshore wind turbines to reduce some ultimate loads. The holistic design optimization of wind turbines mounted on floating substructures are an open engineering and research question.
- 4) High Tilt Angles for Wind Farm Power Maximization: Larger tilt angles in downwind wind turbines would deflect rotor wakes toward the ground and encourage entrainment of wind energy from layers above the wind farm [45,46]. Therefore, highly tilted rotors could increase the total power output of the wind farm by significantly reducing wake losses, which would offset the lower power output of any single turbine. Only downwind turbines are applicable for that. Unexplored combinations of high tilt angles to maximize the swept area and negative cone angles to maximize the swept area could also yield benefits.

## 8. CONCLUSIONS/RECOMMENDATIONS

Extensive studies were conducted for modeling and perspectives of downwind turbines. The representative research achievements and recommendations are summarized as below.

### 1) Tower shadow models for blade aerodynamic loads

Appropriate tower shadow models for BEM are recommended for blade aerodynamic loads are different in accordance with the size and rotor speed.

- Blade loads of large-scale downwind turbines: Load equivalent tower shadow model.
- Blade loads of small downwind turbines: Dynamic tower shadow model for small wind turbines, which is negligible for large scale wind turbines.
- Scaling of downwind turbines: System engineering model to consider the tower shadow effect of downwind turbines.

### 2) Tower shadow models for tower aerodynamic loads.

Following models were recommended for in cases tower shadow loads on the tower are critical.

- Average load: A momentum theory-based model.
- Dynamic load: A lifting line theory-based model.

### 3) Nacelle blockage effect

- However, an engineering model is recommended for the nacelle blockage effect, it is negligible in case of nacelle or spinner is not extremely large.

### 4) Passive yaw idling model and conditions

- As for wind direction, in addition to the short cycle fluctuation calculated from the turbulence model, change rate of average wind direction assumed in storm standby condition is set as constant.
- Yaw misalignment is acquired from of dynamic analysis according to the settings of wind speed, wind direction, wind turbine yaw response and so on.

### 5) Scaling benefits of downwind turbines

- Although energy production would be reduced, lighter blades of downwind turbines were shown to be advantageous for cost reduction.

### 6) Further Opportunities of Downwind Turbines

- Performances, loads, LCOEs of 10 MW upwind and downwind turbines compared through multidisciplinary design, analysis, and optimization studies. The downwind turbine shows 4.4% lower blade mass, with 1.2% higher AEP and 0.9% higher LCOE than the upwind turbine.
- Sensitivity studies show the opportunities for further improvement of LCOE and research opportunities of downwind turbines in 1) aerodynamics of coned and highly flexible rotors, 2) advanced controls, 3) floating offshore wind turbines, 4) high tilt angles for wind farm power maximization.

Further works are necessary to validate these results and verify the proposed recommendations to reflect them in IEC61400-1. And some more information about the 2 MW baseline downwind turbine models and the typical test data of the 2 MW downwind turbine are available in the appendix.

## APPENDIX

### A.1 2 MW Baseline Model

#### A1.1 Outline

Aeroelastic model was defined for a 2 MW downwind turbine.

#### A1.2 Model Data

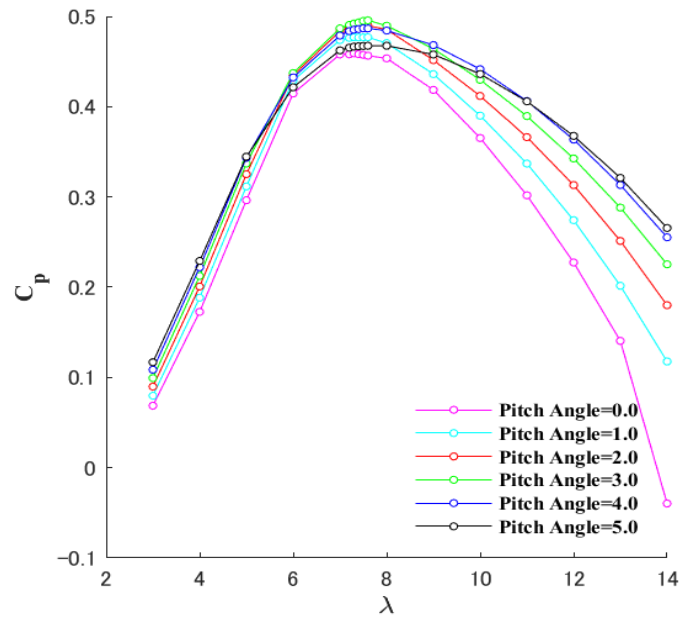
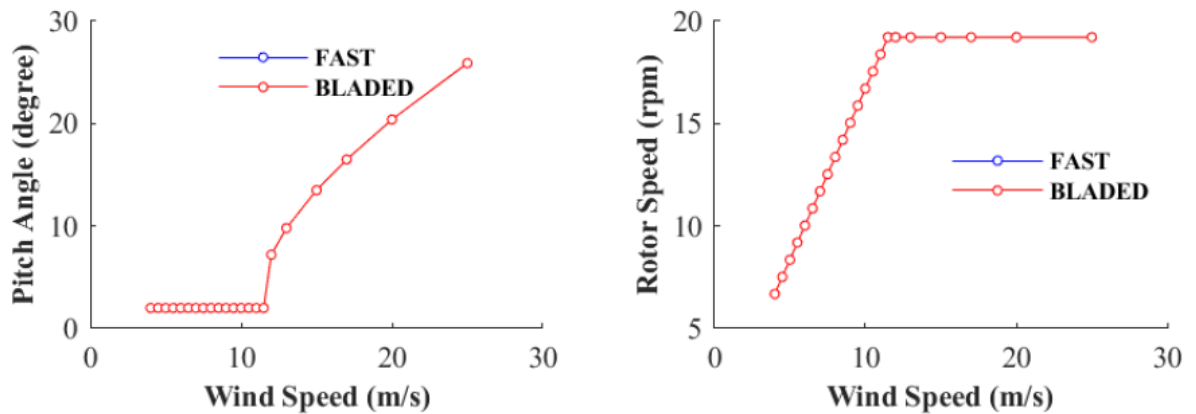


Figure 52 Power coefficients to TSR and pitch angle.



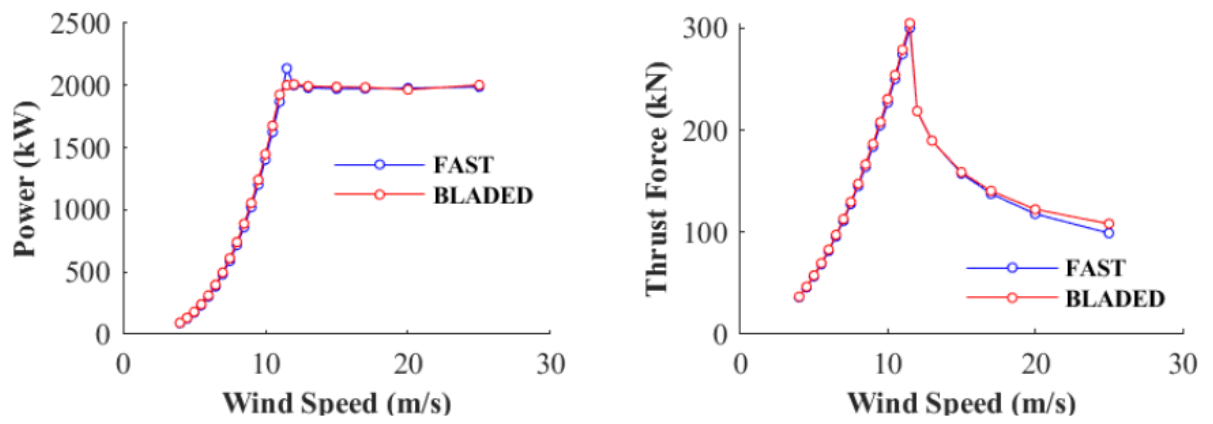


Figure 53 Steady characteristics: (top-left) pitch angle, (top-right) rotor speed, (bottom-left) Power, (bottom-right) thrust

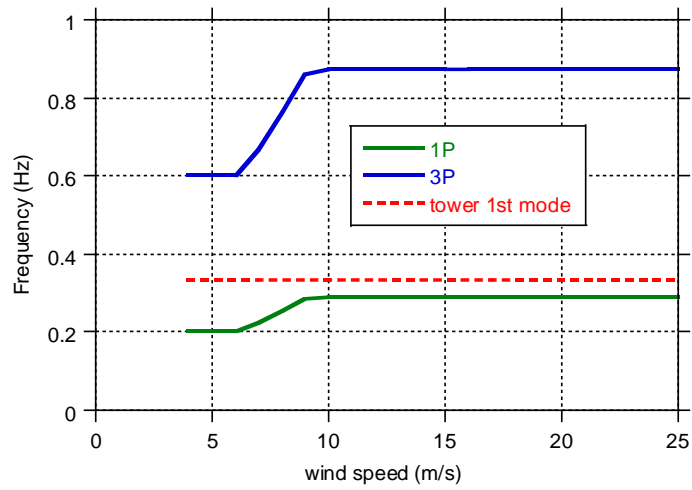


Figure 54 Tower 1st mode frequency to rotor excitation frequency

## A.2 Field Test Data of a 2 MW Downwind Turbine

### A2.1 Outline

- Wind turbine: HTW2.1-80A, Hitachi 2MW DT installed in a flat terrain.
- Measurement data: Operation condition, blade root bending(x2), tower top/bottom bending(x2)

Table 9 Environmental data of the field test

Operation Mode	Power Production	Power Production	Idling
Av. Wind Speed (TI)	8.6 m/s (8.3%)	16.6 (9.2%)	19.9 m/s(5.5%)
Av. Wind Direction	180 deg	306 deg	278 deg
Av. Yaw Angle (Std.)	0.7 deg (7.5 deg)	3.6 deg (7.5 deg)	-1.7 deg (7.5 deg)

### A2.2 Measurement Data

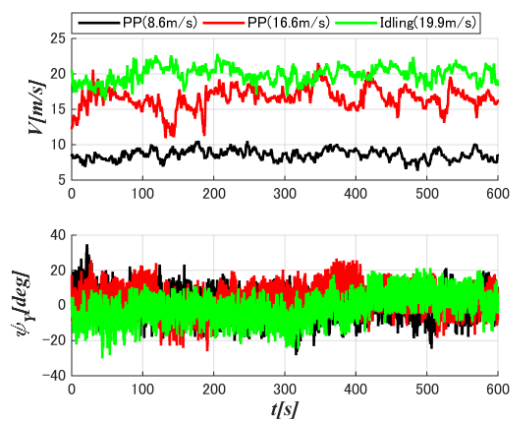


Figure 55 Wind speed and yaw angle

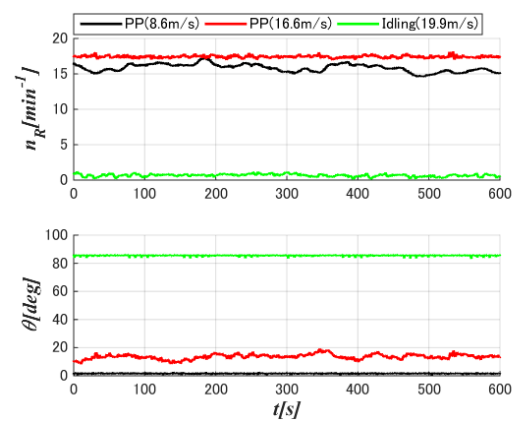


Figure 56 Rotor speed and pitch angle

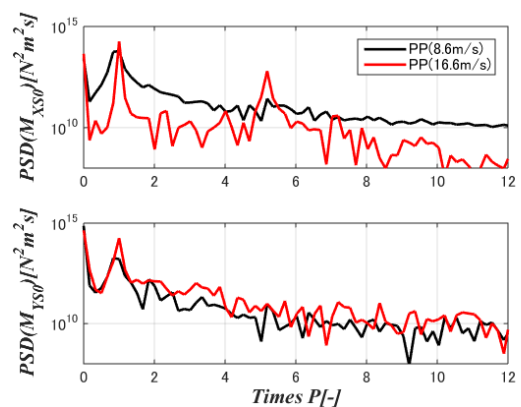
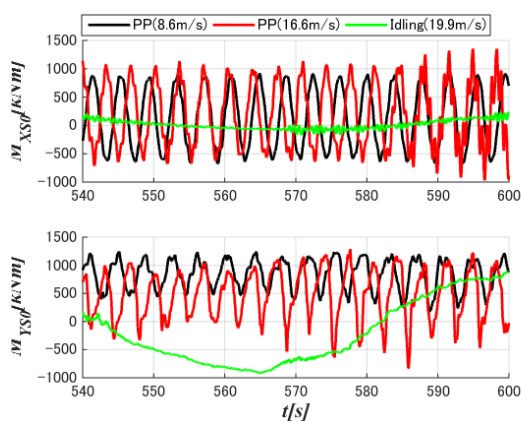


Figure 57 Blade root edgewise/flapwise bending moments

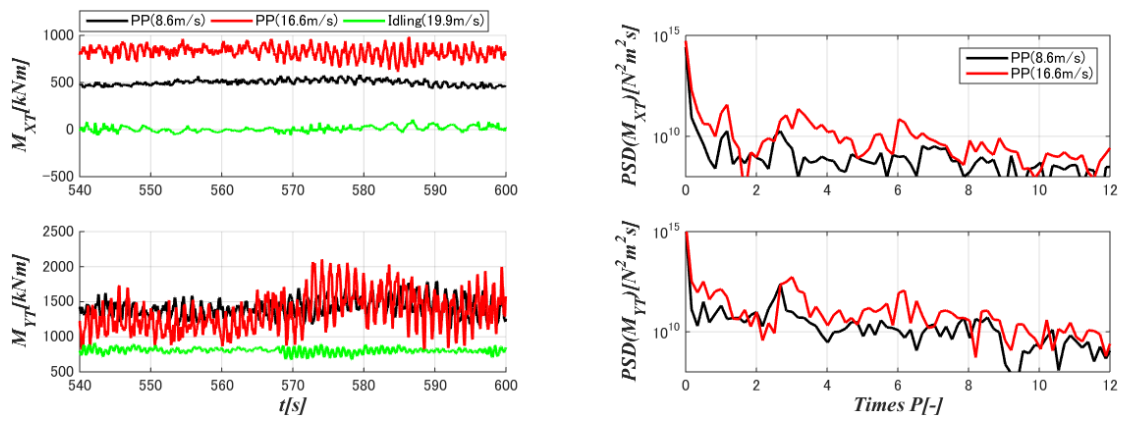


Figure 58 Tower top fore-aft/side-side bending moments

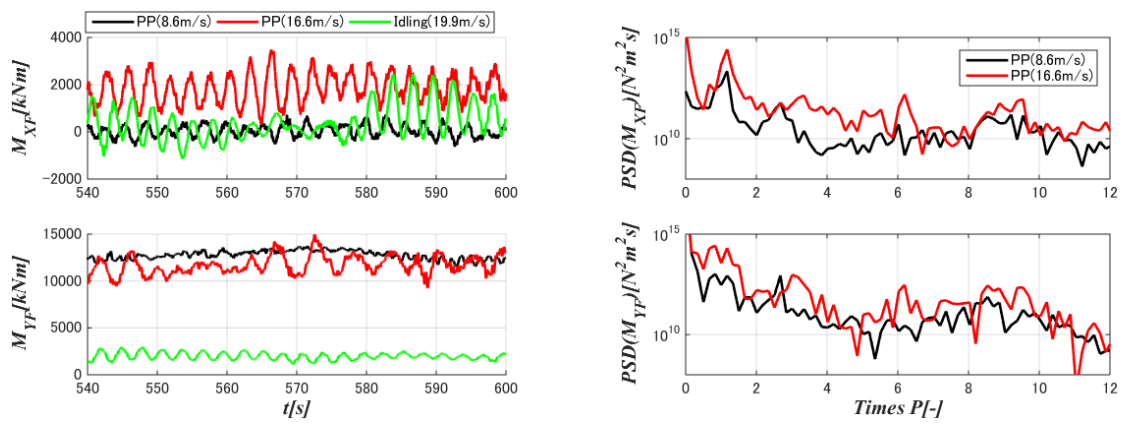


Figure 59 Tower base fore-aft/side-side bending moments

## REFERENCE

- [1] Spera D. editor, Wind Turbine Technology, Fundamental Concepts of Wind Turbine Engineering, ASME Press, New York, 1994.
- [2] Hau E., Wind-Turbines, Fundamentals, Technologies, Applications, Economics, Springer ISBN 3-540-57-64-0, 2000.
- [3] Manwell J., McGowan J., Rogers A., Wind Energy Explained, Theory, Design and Application, Second Edition, Wiley & Sons, 2009.
- [4] Betz, A., Windenergie und ihre Ausnutzung durch Windmuhlen, Gottinger, Germany, Vanderhoeck und Ruprecht, 1926.
- [5] Golding E.W., The Generation of Electricity by Wind Power. London: E. & F.N Spon Ltd; reprinted by R.I. Harris. 1976, New York: Halsted Press, Division of Wiley and Sons, Inc., 1955.
- [6] Hutter U., Die Entwicklung van Windla'aftanlagen zur Stromerzeugung in Deutschland Vol. 6, NF.7, BWK 1954.
- [7] Couturier P.J., Analysis of Tower Shadow Effects and Pre-Aligned Concept for Large Scale Downwind Wind Turbine, Technical University of Denmark, 2014.
- [8] OpenCFD, OpenFOAM, <https://www.openfoam.com/>, Accessed on 2022/03/15.
- [9] Yoshida S., Kiyoki S., Load Equivalent Tower Shadow Modeling for Downwind Turbines, Journal of JSME (B) Vol.73, No.730, 2007, pp.1273-1279.
- [10] Yoshida S., Kiyoki S., Load Equivalent Tower Shadow Modeling, European Wind Energy Conference, 2007.
- [11] ANSYS, ANSYS CFX, Canonsburg, PA, USA, 2006.
- [12] DNV, Bladed, Bristol, UK, 2022.
- [13] Yoshida S., Dynamic Stall Model for Tower Shadow Effects on Downwind Turbines and Its Scale Effects, energies, 10.3390/en13195237, 1-19, Energies 2020, 13, 5237, 2020.
- [14] Munduate X., Coton F.N., Galbraith R.A.M., An Investigation of the Aerodynamic Responses of a Wind Turbine Blade to Tower Shadow, J. Solar Energy Engineering, 126, 1034-1040, 2004.
- [15] Namura N., Shinozaki Y., Design Optimization of 10 MW Downwind Turbines with Flexible Blades and Comparison with Upwind Turbines, J. Phys. Conf. Ser. 1618 042021, 2020.
- [16] National Renewable Energy Laboratory, WISDEM, <https://www.nrel.gov/wind/systems-engineering.html>, Accessed on 2021/11/06.
- [17] Ning A., Petch D., Integrated Design of Downwind Land-based Wind Turbines Using Analytic Gradients, Wind Energy, 19, 2137–52, 2016.
- [18] National Renewable Energy Laboratory, FAST, <https://www.nrel.gov/wind/nwtc/fast.html>, Accessed on 2021/11/22.
- [19] Yoshida S., Combined Blade-Element Momentum - Lifting Line Model for Variable Loads of Downwind Turbine Towers, energies, 11, 2521, 1-18, 2018.
- [20] Yoshida S., Fujii K., Hamasaki M., Takada A., Effect of Rotor Thrust on the Average Tower Drag of Downwind Turbines, energies, 12, 2, 227-241, 2019.
- [21] Anderson B., Branlard E., Vijayakumar, G., Johnson, N., Investigation of the Nacelle Blockage Effect for a Downwind Turbine, J. Phys. Conf. Ser. 1618 062062, 2020.
- [22] International Electrotechnical Commission, IEC6100-1 Wind Energy Generation Systems – Part 1: Design Requirements, ed.4, 2019.
- [23] Namura N., Shinozaki Y., Design Optimization of 10MW Downwind Turbines with Flexible Blades and Comparison with Upwind Turbines, J. Phys. Conf. Ser. 1618 042021, 2020.
- [24] Kiyoki S., Ishihara T., Saeki M., Tobinaga I., Evaluation of Wind Load by Passive Yaw Control at the

- Extreme Wind Speed Condition and Its Verification by Measurement, Proceeding of Grand Renewable Energy 2018 International Conference and Exhibition, 17-22 June (Yokohama), 2018.
- [25] Sartori L., Bortolotti P., Croce A., Bottasso C.L., Integration of Prebend Optimization in a Holistic Wind Turbine Design Tool *J. Phys.: Conf. Ser.* 753 062006, 2016.
- [26] Bortolotti P., Tarr H.C., Dykes K., Merz K., Sethuraman L., Verelst D., Zahle F., IEA Wind Task 37 on Systems Engineering in Wind Energy WP2.1 Reference Wind Turbines, National Renewable Energy Laboratory NREL/TP-5000-73492, 2019.
- [27] Resor B.R., Definition of a 5 MW/61.5 m Wind Turbine Blade Reference Model, Sandia National Laboratories SAND2013-2569, 2013.
- [28] Ichter B., Steele A., Loth E., Moriarty P., Selig M., A Morphing Downwind-aligned Rotor, Concept Based on a 13-MW Wind Turbine, *Wind Energy*, 19, 625-37, 2015.
- [29] Loth E., Steele A., Qin C., Ichter B., Selig M.S., Moriarty P., Downwind Pre-aligned Rotors for Extreme-Scale Wind Turbines, *Wind Energy*, 20, 1241-59, 2017.
- [30] Kiyoki S., Sakamoto K., Kakuya H., Saeki M., 2017 5-MW Downwind Wind Turbine Demonstration and Work toward Smart Operation Control, *Hitachi Review* 66, 5, 38-44, 2017.
- [31] Bortolotti P., Ivanov, H., Johnson, N., Barter, G.E., Veers, P., Namura., Challenges, Opportunities, and a Research Roadmap for Downwind Wind Turbines, *Wind Energy*, 25, 2022, 354–367.
- [32] NREL, ROSCO Version 1.0.0, GitHub repository, 2020.
- [33] NREL, ROSCO Toolbox. Version 1.0.0, GitHub repository, 2020.
- [34] Abbas N.J., Wright A., Pao L., An Update to the National Renewable Energy Laboratory Baseline Wind Turbine Controller, *J Phys Conf Ser.* 2020;1452:012002.
- [35] Bortolotti P., Berry D., Murray R., et al., A Detailed Wind Turbine Blade Cost Model, NREL/TP-5000-73585, 2019.
- [36] NREL, WISDEM, GitHub repository, 2020.
- [37] Stehly, T., Beiter, P., 2018 Cost of Wind Energy Review, NREL/TP-5000-74598, 2019.
- [38] Wanke G., Bergami L., Zahle F., Verelst D.R., Re-design of an Upwind Rotor for a Downwind Configuration: Design Changes and Cost Evaluation, *Wind Energy Sci.* 2021, 6, 203-220.
- [39] Bortolotti P., Kapila A., Bottasso C., Comparison between Upwind and Downwind Designs of a 10 MW Wind Turbine Rotor, *Wind Energy Sci.* 2019, 4(1), 115-125.
- [40] Picot N., Verelst D.R., Larsen T.J., Free Yawing Stall-controlled Downwind Wind Turbine with Swept Blades and Coned Rotor, European Wind Energy Association (EWEA), 2011.
- [41] Wanke G., Hansen M.H., Larsen T.J., Qualitative Yaw Stability Analysis of Free-yawing Downwind Turbines, *Wind Energy Sci.* 2019, 4(2), 233-250, 2019.
- [42] Verelst D., Larsen T., Wingerden V.J.W., Open Access Wind Tunnel Measurements of a Downwind Free Yawing Wind Turbine. *J Phys Conf Series.* 2016, 753:072013.
- [43] Kress C, Chokani N, Abhari R. Downwind Wind Turbine Yaw Stability and Performance, *Renew Energy.* 2015, 83, 1157-1165.
- [44] Shaler K., Branlard E., Platt A., OLAF User's Guide and Theory Manual, NREL/TP-5000-75959, 2020.
- [45] Annoni J., Scholbrock A., Churchfield M., Fleming P., Evaluating Tilt for Wind Plants, 2017 American Control Conference (ACC), 2017, 717-722.
- [46] Cossu C., Replacing Wakes with Streaks in Wind Turbine Arrays, *Wind Energy*, 24(4), 2021, 345-356.